Systems/Circuits

Neuromedin B-Expressing Neurons in the Retrotrapezoid Nucleus Regulate Respiratory Homeostasis and Promote Stable Breathing in Adult Mice

George M.P.R. Souza, Daniel S. Stornetta, Yingtang Shi, Eunu Lim, Faye E. Berry, Douglas A. Bayliss, and Stephen B.G. Abbott

Department of Pharmacology, University of Virginia, Charlottesville, Virginia 22908

Respiratory chemoreceptor activity encoding arterial P_{CO_2} and P_{O_2} is a critical determinant of ventilation. Currently, the relative importance of several putative chemoreceptor mechanisms for maintaining eupneic breathing and respiratory homeostasis is debated. Transcriptomic and anatomic evidence suggests that bombesin-related peptide Neuromedin-B (*Nmb*) expression identifies chemoreceptor neurons in the retrotrapezoid nucleus (RTN) that mediate the hypercapnic ventilatory response, but functional support is missing. In this study, we generated a transgenic *Nmb*-Cre mouse and used Cre-dependent cell ablation and optogenetics to test the hypothesis that RTN^{Nmb} neurons are necessary for the CO_2-dependent drive to breathe in adult male and female mice. Selective ablation of ~95% of RTN^{Nmb} neurons causes compensated respiratory acidosis because of alveolar hypoventilation, as well as profound breathing instability and respiratory-related sleep disruption. Following RTN^{Nmb} lesion, mice were hypoxemic at rest and were prone to severe apneas during hyperoxia, suggesting that oxygen-sensitive mechanisms, presumably the peripheral chemoreceptors, compensate for the loss of RTN^{Nmb} neurons. Interestingly, ventilation following RTN^{Nmb}-lesion was unresponsive to hypercapnia, but behavioral responses to CO_2 (freezing and avoidance) and the hypoxia ventilatory response were preserved. Neuroanatomical mapping shows that RTN^{Nmb} neurons are highly collateralized and innervate the respiratory-related centers in the pons and medulla with a strong ipsilateral preference. Together, this evidence suggests that RTN^{Nmb} neurons are dedicated to the respiratory effects of arterial P_{CO_2}/pH and maintain respiratory homeostasis in intact conditions and suggest that malfunction of these neurons could underlie the etiology of certain forms of sleep-disordered breathing in humans.

Key words: blood gas homeostasis; carotid body; central chemoreceptor; periodic breathing; sleep homeostasis sleep-disordered breathing

Significance Statement

Respiratory chemoreceptors stimulate neural respiratory motor output to regulate arterial P_{CO_2} and P_{O_2}, thereby maintaining optimal gas exchange. Neurons in the retrotrapezoid nucleus (RTN) that express the bombesin-related peptide Neuromedin-B are proposed to be important in this process, but functional evidence has not been established. Here, we developed a transgenic mouse model and demonstrated that RTN neurons are fundamental for respiratory homeostasis and mediate the stimulatory effects of CO_2 on breathing. Our functional and anatomic data indicate that *Nmb*-expressing RTN neurons are an integral component of the neural mechanisms that mediate CO_2-dependent drive to breathe and maintain alveolar ventilation. This work highlights the importance of the interdependent and dynamic integration of CO_2- and O_2-sensing mechanisms in respiratory homeostasis of mammals.

Introduction

Breathing is a highly coordinated motor activity that serves the essential function of maintaining blood gas homeostasis (Del Negro et al., 2018). In mammals, central and peripheral respiratory chemoreceptors regulate lung ventilation in relation to arterial P_{CO_2} and P_{O_2} (Nattie and Li, 2012; Del Negro et al., 2018; Guyenet and Bayliss, 2022). Depending on species and approach, central respiratory chemoreceptors that encode CO_2 and H^+ generate between 50% and 70% of resting ventilation derived from arterial P_{CO_2} (Pa_{CO_2}) at baseline (Blain et al., 2009; Smith et al., 2010; Guyenet et al., 2018). Although several cell types have

Received Feb. 28, 2023; revised June 1, 2023; accepted June 5, 2023.

Author contributions: G.M.P.R.S., D.A.B., and S.B.G.A. designed research; G.M.P.R.S., D.S.S., E.L., F.E.B., and S.B.G.A. performed research; G.M.P.R.S., D.S.S., E.L., F.E.B., and S.B.G.A. analyzed data; G.M.P.R.S. and S.B.G.A. wrote the first draft of the paper; G.M.P.R.S. and S.B.G.A. wrote the paper; D.S.S. and D.A.B. edited the paper; Y.S. and D.A.B. contributed unpublished reagents/analytic tools.

This work was supported by National Institutes of Health Grant HL108609 to D.A.B. and HL148004 to S.B.G.A.; and CCHS Family Foundation Pilot Grant to Y.S. We thank Dr. Patrice Guyenet for helpful feedback throughout the course of this project.

The authors declare no competing financial interests.

Correspondence should be addressed to Stephen B.G. Abbott at sba6t@virginia.edu.

https://doi.org/10.1523/JNEUROSCI.0386-23.2023

been suggested to function as central respiratory chemoreceptors, the hierarchical and functional interdependence of these chemoreceptors for eupneic breathing and CO_2 homeostasis is still a matter of debate (Nattie and Li, 2012; Guyenet et al., 2019; Gourine and Dale, 2022).

A prominent group of central respiratory chemoreceptors are retrotrapezoid nucleus (RTN) neurons. RTN neurons are excitatory, CO_2-activated neurons located in the parafacial region derived from a developmental lineage that includes *Egr-2*, *Lbx1*, *Atoh-1*, and importantly, *Phox2b* as key markers (Guyenet et al., 2019; Guyenet and Bayliss, 2022). Polyalanine expansion mutations in Phox2b are associated with congenital central hypoventilation syndrome (CCHS) in humans, a rare genetic condition characterized by hypoventilation and apnea during sleep (Amiel et al., 2003; Weese-Mayer et al., 2010). Developmental studies modeling CCHS-like mutations in mice show that an absence of RTN neurons might explain the deficits in the hypercapnic ventilatory reflex (HCVR) in humans with CCHS (Dubreuil et al., 2009; Ramanantsoa et al., 2011; Ruffault et al., 2015). However, resting breathing and the HCVR in mice with CCHS-like mutations partly recover during development, raising important questions of the role of the RTN in adults. Experimental studies in unanesthetized adult rats provide varied evidence. For example, acute and reversible optogenetic inhibition of a mixed population of RTN and nearby C1 neurons reduces breathing by ~40% during waking and non-rapid eye movement sleep (NREMS) (Burke et al., 2015). Similarly, ablation of RTN neurons using saporin, a ribosomal toxin, targeted to tachykinin receptor 1-expressing cells in the parafacial region causes alveolar hypoventilation and blunts the HCVR (Takakura et al., 2014; Souza et al., 2018). However, others have shown that chemogenetic inhibition of RTN neurons produces a negligible effect on resting ventilation and does not attenuate diaphragmatic activity during hypercapnia (Marina et al., 2010). Thus, while there is a general agreement that RTN neurons contribute to the increase in pulmonary ventilation in response to CO_2, it remains uncertain whether these neurons contribute to eupneic (i.e., resting) ventilation in adults.

In rodents, putative central chemoreceptor neurons in the RTN can be identified by the expression of a constellation of markers, including expression of Phox2b, vesicular glutamate transporter 2 (*Slc17a6*), tachykinin receptor 1 (TACR1), galanin, and more recently neuromedin B (*Nmb*), as well as the absence of TH and ChAT (Guyenet et al., 2019; Guyenet and Bayliss, 2022). Among these identifiers, *Nmb*, first described by Li et al. (2016), is universally expressed in putative central chemoreceptor neurons of the RTN (Shi et al., 2017), although evidence linking these neurons with respiratory homeostasis is lacking. Importantly, between 80% and 90% of *Nmb* neurons in the parafacial region express GPR4 and TASK2 (Shi et al., 2017), which are acid-sensitive proteins that are critical for the HCVR (Gestreau et al., 2010; Kumar et al., 2015). Thus, we hypothesized that *Nmb* expression identifies central chemoreceptor neurons in the RTN that contribute to respiratory homeostasis. We tested this hypothesis by generating a transgenic *Nmb*-Cre knock-in mouse in which we used genetically targeted cell ablation and optogenetic techniques to determine the contribution of the RTN^{Nmb} neurons to the control of breathing in adult mice.

Materials and Methods

Animals. All experiments were conducted in accordance with the National Institutes of Health's *Guide for the care and use of laboratory animals* and approved by the University of Virginia Animal Care and Use Committee (protocol #4312). We used transgenic $Nmb^{Cre/+}$ male and female mice. These mice were generated by homologous recombination in embryonic stem (ES) cells to introduce an IRES-Cre cassette into the *Nmb* locus by Ingenious Targeting Laboratory. In short, an 11.9 kb genomic DNA was extracted from a positively identified C57BL/6 BAC clone (RP23-425N1) and inserted into a ~2.4 kb pSP72 (Promega) backbone vector. The inserted region included homology arms 5′ (3.2 kb) and 3′ (8.5 kb) relative to the knock-in cassette. The knock-in cassette containing IRES-Cre-pA and FRT-flanked neomycin resistance (Neo) cassette was inserted immediately downstream of the TAG stop codon in exon 3 of the mouse *Nmb* gene. The targeting vector was confirmed by restriction analysis and sequencing after each modification step. The targeting vector was linearized (NotI) and transfected by electroporation of FLP C57BL/6 (BF1) ES cells, selected with G418 antibiotic, and surviving clones were expanded for PCR analysis to identify recombinant ES clones and verify FLP-mediated excision of the Neo cassette. Correctly targeted iTL BF1 (C57BL/6 FLP) ES cells were microinjected into BALB/c blastocysts, and resulting chimeric mice were mated to C57BL/6N WT mice to generate germline mice. PCR products from tail DNA were sequenced to verify proper targeting and a separate PCR confirmed absence of FLP recombinase. The *Nmb*-Cre mouse line was maintained in house by crossing with C57BL/6J mice acquired from The Jackson Laboratory (stock #000664), and male and female WT control ($Nmb^{+/+}$) and heterozygous Cre-positive littermates ($Nmb^{Cre/+}$) were used for experiments.

For anatomic studies, we used $Nmb^{Cre/+}$::Jx99 mice generated by crossing $Nmb^{Cre/+}$ mice with JX99 (Phox2b::eGFP BAC transgenic) mice on a mixed genetic background (Lazarenko et al., 2009). For retrograde tracing studies, we used R26-loxSTOPlox-L10-GFP Cre-reporter mice acquired from The Jackson Laboratory (strain #024750, RRID: IMSR_JAX:024750) and bred as heterozygotes with C57BL/6J mice in house. Animals were group-housed wherever possible and maintained under a 12:12 light: dark cycle (lights on at 700 h) at 23°C-24°C with water and food provided *ad libitum*.

Viral vectors. For the mouse model validation, we tested the selectivity of the viral vector transduction using microinjection of Cre-dependent vector containing the fluorophore mCherry (AAV_2-hSyn-DIO-hM3D(Gq)-mCherry, Addgene plasmid 44361, titer: 8.0×10^{11} GC/ml). To promote RTN^{Nmb} ablation, we used a Cre-dependent vector (AAV_5-FLEX-taCasp3-TEVp, titer: 4.2×10^{12} GC/ml, University of North Carolina Vector Core). This vector expresses the apoptotic enzyme caspase-3 (taCasp3) and its activation protease, the Tobacco Etch Virus protease (TEVp) in Cre-expressing cells. To identify efferent connections from RTN^{Nmb} neurons, we used a vector containing the fluorophore mScarlet (AAV_8-nEF-Con/Foff 2.0-ChRmine-oScarlet, titer for injection: 1.2×10^{12} GC/ml, Addgene plasmid 137161) (Fenno et al., 2020). For retrograde tracing, we used a retrograde vector expressing Cre-recombinase (AAV_{rg}-hSyn-Cre-WPRE-hGH, Addgene plasmid 105553, titer: 2.39×10^{13} GC/ml). For optogenetic inhibition of RTN^{Nmb} neurons, we used eArch3.0 (AAV_2-EF1α-DIO-eArch3.0-eYFP, UNC Vector Core, titer for injection: 4.0×10^{12} GC/ml).

Animal preparation and brainstem microinjections. Mice of both sexes (age: 8-12 weeks) were anesthetized with a mixture of ketamine (100 mg/kg) and dexmedetomidine (0.2 mg/kg) given intraperitoneally. The depth of anesthesia was assessed by an absence of the hind-paw withdrawal reflex. Additional anesthetic was administered as necessary (20% of the original dose, i.p.). The following procedures were performed under aseptic conditions. Following skin shaving and disinfection, the skin overlying the left mandible was cut to reveal a short segment of the mandibular branch of the facial nerve. The mice were then placed on a stereotaxic apparatus adapted for mouse CNS microinjections (ear bar adaptor, model EB-5N, Narashige Scientific Instrument Lab; bite bar, model 926 mouse adaptor set at −3 mm below the interaural line for a flat skull, David Kopf Instruments). Body temperature maintained at 37°C with a servo-controlled heating pad and a blanket. A small hole, 1.5 mm in diameter, was drilled bilaterally into the occipital plate caudal to the parieto-occipital suture. The AAV was loaded into a 1.2 mm internal diameter glass pipette broken to a 25 µm tip (external

diameter). The facial nerve was stimulated (0.1 ms, 100-300 μA, 1 Hz) to evoke antidromic field potentials within the facial motor nucleus as previously described (Abbott et al., 2013). These field potentials were used to map the facial motor nucleus and help identify the location of the RTN neurons, which reside 100-200 μm below this nucleus.

For the ablation of RTN^{Nmb} neurons, microinjections of AAV_5-FLEX-taCasp3-TEVp, 60-80 nl of virus were delivered bilaterally at three sites spanning the rostro-caudal length of the facial nucleus (1400 μm lateral, 100 μm below the bottom of the facial nucleus). For tracing and selectivity experiments, two 50 nl injections of virus (AAV_8-nEF-Con/Foff 2.0-ChRmine-oScarlet or AAV_2-EF1α-DIO-eArch3.0-eYFP) were placed underneath the facial nucleus. For retrograde tracing studies, <10-20 nl of virus AAV_{rg}-hSyn-Cre was placed at the following coordinates relative to λ: pre-Bötzinger complex (PreBötC) at −2.7 mm caudal, 1.25 mm lateral, 4.5 mm ventral of brain surface; and lateral parabrachial nucleus (LPB) at −0.6 mm caudal, 2.1 mm lateral, 3.5 mm ventral of brain surface. The caudal ventral respiratory group (cVRG) and nucleus of the solitary tract (NTS) were accessed via an atlanto-occipital window with the nose of the mouse 5 mm below a flat-skull position. Coordinates relative to obex were as follows: cVRG at 0.0 mm caudal, 1.2 mm lateral, 2.5 mm ventral of brain surface; and NTS at 0.0 mm rostral, 0.1 mm lateral, 0.25 mm ventral of brain surface. For the optogenetic loss-of-function experiments, a vector encoding eArch3.0 (AAV_2-EF1α-DIO-eArch3.0-eYFP) was microinjected in the left RTN in three sites spanning the rostro-caudal length of the facial nucleus (1400 μm lateral to midline, 100 μm below the bottom of the facial nucleus) and a vector encoding taCasp3 (AAV_5-FLEX-taCasp3-TEVp) was injected in the contralateral RTN in the same fashion. This experimental approach produces unilateral ablation of RTN^{Nmb} neurons allowing a more pronounced effect of the optogenetic inhibition of the contralateral side on the respiratory variables.

In all mice, incisions were closed with sutures and surgical cyanoacrylate adhesive. Mice received postoperative boluses of atipamezole (α_2-adrenergic antagonist, 2 mg/kg, s.c.) and ketoprofen (4 mg/kg, s.c.) and were then placed in a clean warmed home cage (37°C) until consciousness was regained before being returned to the vivarium. Ketoprofen was administered immediately after surgery and at 24, 48, and 72 h following surgery. Mice were housed in the vivarium for >4 weeks before experimentation to allow sufficient expression of the transgene and/or caspase-mediated cell death.

Arterial blood gases. Arterial blood gases were assessed during quiet breathing in unrestrained, conscious mice by blood withdrawal from an arterial catheter. Two days before the experiment, mice were anesthetized with isoflurane (2.5% in normoxia) and a polyethylene catheter (PE-8 connected to a PE-50) was inserted in the abdominal aorta through the femoral artery. The catheter was tunneled under the skin and the tip placed in the dorsal aspect of the neck. This procedure lasted 10-15 min, and ketoprofen was administered after the surgery (4 mg/kg, s.c). After 2 d, mice were placed in the plethysmography chamber, and blood samples were withdrawn (100 μl) and filled into hand-held i-STAT 1 configured with $CG4^+$ cartridges for analysis. After this procedure, mice were deeply anesthetized with a mixture of ketamine (200 mg/kg) and dexmedetomidine (0.4 mg/kg) given intraperitoneally and transcardially perfused for histologic examination. Blood samples were obtained exclusively in male mice because of their larger size and greater success rate of the femoral arterial catheter implant surgery. The implant was performed via the femoral artery rather than the carotid artery to avoid disturbing carotid body function.

Metabolic activity. Mice were placed in a plexiglass chamber (15 cm × 10 cm × 10 cm) connected to a Comprehensive Lab Animal Monitoring System with a continuous flow of 0.5 L/min of normoxia (Columbus Instruments). Mice were provided *ad libitum* food and water and had access to enrichment, including nesting materials. Recording sessions occurred over a period of at least 4 d with data acquired in the final 24 h of recording used for analysis. Body temperature was measured in a subset of mice by introducing a rectal probe connected to a temperature monitor.

Unrestrained whole-body plethysmography and respiratory challenges. Breathing parameters were evaluated in conscious unrestrained mice using whole-body plethysmography (400 ml internal volume, Data Sciences International). Recording sessions were conducted between 0900 and 1600 h and lasted <6 h. Chambers were continuously flushed with dry room temperature air delivered by three computer-driven mass flow regulators controlling the flow of O_2, N_2, and CO_2 (total flow: 1 L/min/chamber). An estimation of tidal volume (V_T) was calibrated to air injected into the plethysmography chamber from a 1 ml syringe. The flow signal was amplified (×200) and acquired at 1 kHz in Spike2 software (version 9, CED).

In this study, mice were exposed to different respiratory challenges, such as hyperoxic hypercapnia, normoxic hypercapnia, and hypoxia to test specific hypotheses. For the hyperoxic hypercapnia protocol, the inspired fraction of oxygen (F_IO_2) increased initially from 0.21 to 0.60 and then stayed at this level during the whole protocol, similar to our previous studies (Souza et al., 2018). After 10 min of hyperoxia, the inspired fraction of CO_2 (F_ICO_2) increased from 0 to 0.03, followed by an increase of F_ICO_2 to 0.06 and finally an increase in F_ICO_2 to 0.09. Each of the three episodes of hypercapnia lasted 10 min and was followed by recovery in normoxia for at least 20 min. For the normoxic normocapnia, the same step changes in F_ICO_2 described above were conducted in normoxia (F_IO_2 = 0.21). The hypoxia protocol was performed by exposing the mice to F_IO_2 = 0.1 for 10 min, following a period of normoxia recovery (reoxygenation) for 20 min before a second exposure to hypoxia F_IO_2 = 0.12 for 10 min.

Respiratory frequency (f_R) and V_T were analyzed from periods free of movement artifacts, and minute ventilation (V_E) was calculated as a product of $f_R \times V_T$. For the analysis of breathing during sleep, these variables were analyzed as the average of 5 segments of ~40-120 s duration each. The variability of breathing was calculated as the percentage change in the duration of a given respiratory cycle in relation to its preceding one. The breathing variability index was calculated using at least 100 breaths for each condition. The apnea index was calculated as the proportion of breathing pauses that lasted >1 s among a given number of respiratory cycles (number of apneas/number of breaths). During hypercapnia and hypoxia, the analysis of V_T, f_R, and breathing variability was performed at 7-10 min from the beginning of the gas change. The ventilatory response to hyperoxia was determined from data between 30 and 60 s and also 7-10 min from the onset of the stimulus. To determine the sensitivity of the hypercapnic ventilatory response, linear regression was performed to determine the slope of the ventilatory response for each animal and condition. We removed three data points from group data in this analysis because the goodness of fit (R^2) was <0.50.

Sleep-wake recordings. Mice were instrumented with six-pin connectors (Mill-Max Manufacturing) connected to three intracranial screws (left frontal, left and right parietal) for EEG recording and two braided stainless-steel wires (A-M Systems) implanted in the neck muscles for EMG recording. EEG (recorded between the left frontal and right parietal screw) and EMG recording were used to monitor sleep behavior. Immediately before the experiment, mice were briefly anesthetized with isoflurane (1.5% in normoxia) to connect the headset. The lead of the headset passed through the top of the plethysmography chamber and connected to the amplifier. EEG and EMG signals were amplified and bandpass filtered (bandpass filter, gain and sampling rate, EEG: 0.1-100 Hz, ×2000, 1 kHz; EMG: 300-1000 Hz, ×300, 1 kHz). All signals were acquired, processed, and analyzed using Spike2 software (CED).

A script available for Spike2 software (sleepscore version 7.05, CED) was used to determine sleep-wake behavior. Sleep-wake behavior was assessed over a continuous 4 h period between 1100 and 1600 h in plethysmography chambers. Sleep-wake state was determined for nonoverlapping 20 s epochs that were manually scored as wake, NREMS, or rapid eye-movement sleep (REMS) by a trained blinded observer based on EEG and EMG activity only. Breathing patterns were not used for scoring sleep-wake state. Micro-arousals, defined as periods of EEG desynchronization lasting between 3 and 9 s with or without EMG activation, were scored during a 10 min period of uninterrupted NREM sleep based on the above sleep-wake state scoring procedure.

Optogenetics. During microinjection surgery (described above), an optical fiber (200 μm core, 0.39 NA) was implanted 500 μm above the left microinjection site in the caudal aspect of the RTN. Postoperative

care was conducted as described above. One month after the surgery, mice were briefly anesthetized with isoflurane (2.0% in normoxia) for the connection of the optical fiber with the laser source and the EEG/EMG headset. The animals were then placed in a plethysmography chamber, and the experiments were conducted 1 h after this procedure in freely behaving mice. We used a green laser (532 nm, 10 mW at the tip of the fiber, 5 s constant pulse) to activate eArch3.0 and, thus, inhibit RTN^{Nmb} neurons. eArch3.0 has been proven to be highly effective at inhibiting RTN^{Nmb} neuron activity in rats (Basting et al., 2015). Ventilatory variables (f_R, V_T, V_E) were analyzed for 5-10 s before the laser stimulation for baseline and then during the 5 s laser stimulation trial. Data points in Figure 7 reflect the average of at least three trials per condition.

CO_2-induced freezing behavior assay. Freezing behavior during exposure to CO_2 was evaluated in an opaque white plastic chamber with a transparent roof (30 cm × 30 cm × 30 cm) to permit video recording from above. RTN^{Nmb}-lesion and control mice were exposed to two conditions on the same day in randomized order, with a period of at least 1 h between tests in each mouse. Mice were not habituated to the chamber before experiments but had been exposed to CO_2 during previous plethysmography sessions. The two conditions tested were normoxia (F_IO_2 = 0.21, F_ICO_2 = 0.00) and 10% hypercapnia (F_IO_2 = 0.21, F_ICO_2 = 0.10), which were generated using mass flow controllers producing a total flow of 5 standard liters per minute (SLPM). CO_2 concentrations were continuously monitored 10 cm above the chamber floor using a capnometer (Columbus Instruments) to ensure F_ICO_2 during the hypercapnia condition was within a range of 9.5% and 10% at the time of placing the mouse in the test chamber and throughout the test, which lasted 5 min, after which mice were returned to their home-cage. The test chamber was cleaned with soapy water and dried between animals. Video data were collected using a consumer web camera attached to a fixed arm 60 cm centered above the chamber floor. Videos were manually calibrated, and no correction was made for lens distortion (Panadeiro et al., 2021). Rodent positions were extracted from videos using a custom data processing pipeline using the OpenCV library (Bradski, 2000). In brief, raw videos were cropped for content, a Gaussian blur was applied, the contents were filtered based on HSV-color values (leveraging the contrast between the black coats of the subject animals and the white plastic environment), and lastly the x and y coordinates of the centroid of the identified contour were used to represent the animal's position. Before analysis, videos and activity traces were manually reviewed for accuracy. Freezing time was determined as periods when the x-y coordinates of the centroid were static. Jumping was manually counted by a scorer blinded to condition.

CO_2-avoidance assay. To assess CO_2 avoidance, we built a custom apparatus consisting of two plastic chambers (30 cm × 30 cm × 30 cm) connected by a passageway (opening 5 cm × 5 cm) with a removable transparent lid. We delivered normoxia and high CO_2 to either side of the apparatus at a flow rate of 5 L/min for each; we also had a scavenging system drawing ~8-10 L/min from a small opening in the passageway to reduce gas mixing between chambers. CO_2 concentration was monitored continuously 5 cm above the chamber floor in the CO_2 chamber using a capnometer (Columbus Instruments), F_ICO_2 values during the experiment in the CO_2 chamber varied between 0.08 and 0.09. To achieve these values, we manually adjusted the concentration of CO_2 administered to the chamber within a range of 12%-15%. Periodic measurements of CO_2 in the normoxia-infused chamber indicate that CO_2 concentrations were <1% in this chamber during experiments. RTN^{Nmb}-lesion and control mice were subject to a single exposure lasting 30 min after which mice were returned to their home-cage. Mice were initially placed in the normoxic chamber and allowed to explore the apparatus freely during the session. Mice were not habituated to the chamber before experiments but had been exposed to CO_2 during previous plethysmography sessions. Separate groups of mice were used for the freezing assay and CO_2 avoidance assay. Video data were collected in the same manner as for the CO_2-induced freezing assay. Avoidance was assessed in 5 min epochs and expressed as time spent in the CO_2 infused-chamber as a percentage of each epoch.

Perfusion and histology procedures. Mice were deeply anesthetized with a mixture of ketamine (100 mg/kg) and dexmedetomidine (0.2 mg/kg) given intraperitoneally and perfused transcardially with 4% PFA, pH 7.4 in 100 mM PB or pH-buffered 10% formalin, pH 7.0. Brains were removed and postfixed in the same fixative for 12-24 h at 4°C. Brains were sectioned (30-50 µm) on a vibratome (VT-1000S, Leica Biosystems), and sections were stored in cryoprotectant (30% ethylene glycol (v/v), 20% glycerol (v/v), 50% 100 mM PB, pH 7.4) at −20°C. Immunohistochemistry was performed on free-floating sections at room temperature unless noted otherwise. Serial 1-in-3 sections were rinsed, then blocked in a solution containing 100 mM Tris, 150 mM saline, 10% horse serum (v/v), 0.1% Triton-X (v/v), and incubated with primary antibodies for 60 min at room temperature then 4°C overnight. Sections were subsequently rinsed and then incubated with secondary antibodies for 60 min at room temperature and rinsed again before mounting on slides. Slides were covered with ProLong Gold anti-fade mounting medium (P36931, Fisher Scientific).

Multiplex FISH was performed using RNAscope (version 1 kit, Advanced Cell Diagnostics). Serial 1-in-3 sections were washed in RNase-free PBS, mounted on charged slides, dried overnight, and processed according to the manufacturer's instructions. When necessary, immunohistochemistry was performed on the slide after the RNAscope procedure using antibodies against mCherry or GFP along with their respective secondary antibodies. Immediately following the RNAscope procedure, sections were rinsed and then incubated in blocking solution for 10 min followed by incubation in primary at room temperature for 60 min, rinsed and incubated in secondary antibodies for 30 min, rinsed and then dried overnight before coverslipping. Slides were coverslipped with Prolong Gold antifade mountant with DAPI (P3693, Fisher Scientific). Primary and secondary antibodies and FISH probes used are detailed in Table 1.

Microscopy, imaging, and cell mapping. Neuronal mapping was conducted using Neurolucida software (MBF Bioscience) with an AxioImager M2 microscope (Carl Zeiss Microscopy). Digital images were acquired in grayscale using a Hamamatsu C11440 Orca-Flash 4.0LT digital camera (Hamamatsu). Maximum projections of z-stack images were exported (8-bit) and further image modifications were performed in ImageJ/Fiji software (Schindelin et al., 2012). Representative images were pseudo-colored and optimized for presentation, brightness, and contrast were adjusted equally in all pixels of the image. Cell counting was conducted with a 1-in-3 series that was subsequently aligned to Paxinos and Franklin's fourth edition (Franklin and Paxinos, 2013). Expression of GFAP was assessed based on brightness of the immunofluorescence staining. The tissue was processed in parallel and imaged with a 20× objective using a camera exposure of 200 ms. Stack images were acquired (10 images with a spacing of 1 µm) and exported as a maximum projection image. Maximum projection images were batch processed in ImageJ/Fiji. In brief, images were manually cropped to the relevant anatomic region, a Gaussian blur was applied, the default auto thresholding was applied (Ridler and Calvard, 1978), despeckled, and then the default particle analysis tool was used to collect signal intensities. Data are expressed in arbitrary units.

To determine the density of axonal varicosities, we counted mScarlet-labeled axonal enlargements (1-3 µm in diameter) in a single area of interest defined anatomically in 3 cases using an oil-immersion 63× objective. The number of varicosities was first normalized to the area of tissue analyzed (range: 10,000-40,000 μm^2) and this value (expressed in density/100 μm^2) was normalized to the number of mScarlet-labeled neurons in each case. To evaluate retrograde-labeling of RTN neurons, we counted all *Nmb*, *Gal*, and GFP-labeled neurons within the ventrolateral medulla between −5.47 and −5.79 mm relative to bregma. GFP fluorescence in neurons and glia at the site of AAV_{rg}-Cre injections was mapped as a representation of injection sites in Figure 10*B*.

Statistics

Data were tested for normality using the D'Agostino–Pearson, Shapiro–Wilk, or Kolmogorov–Smirnov test. Datasets that were considered normally distributed based on at least one of the above-mentioned tests were analyzed using parametric tests, and non-normal distributed

Table 1. Primary and secondary antibodies used for immunohistochemistry and probes used for ISH[a]

Host	Target	Dilution	Vendor	Catalog	RRID
Primary antibodies					
Chicken	GFP	1:1k	Aves Labs	GFP-1020	AB_10000240
Goat	Phox2b	1:100	R&D Systems	AF4940	AB_10889846
Rabbit	DsRed	1:1k	Takara Bio	632496	AB_10013483
Rat	GFAP	1:1k	Thermo Fisher Scientific	13-0300	AB_2532994
Sheep	TH	1:1k	MilliporeSigma	AB1542	AB_90755

Host	Target	Dilution	Fluorophore	Catalog	RRID
Secondary antibodies					
Donkey	Chicken IgY	1:500	488	703-545-155	AB_2340375
Donkey	Rabbit IgG	1:500	Cy3	711-165-152	AB_2307443
Donkey	Sheep IgG	1:500	647	713-606-147	AB_2340752
Donkey	Goat IgG	1:500	488	705-546-147	AB_2340430

Transcript	Catalog	Target Region (bp)	Accession Number
ISH probes			
Dbh	407851	315-1296	NM_138942.3
Nmb	459931	14-685	NM_001291280.1
Tph2	318691	1640-2622	NM_173391.3

[a]All secondary antibodies were purchased from Jackson ImmunoResearch Laboratories. All ISH probes were purchased from Advanced Cell Diagnostics.

samples were analyzed using nonparametric tests. For normally distributed data, Student's *t* test, one-way or two-way ANOVA, usually with repeated measures, followed by Tukey's, Bonferroni's, or Holm–Sidak's multiple comparisons test. The *F* and *p* values for every effect and interaction between effects are reported in the figure legends. The non-normally distributed data were analyzed using Kruskal–Wallis nonparametric test, followed by Dunn's *post hoc* multiple comparisons test or the Mann–Whitney test as specified for each dataset in the figure legends. Differences were considered significant when $p < 0.05$. In figures, data from each animal are presented in scatter plots, with summary data in text shown as mean ± SD unless noted otherwise.

Results

Validation of *Nmb*-Cre mouse and effect of selective-cell ablation on alveolar ventilation at rest

We generated a knock-in transgenic *Nmb*-Cre strain to selectively target RTN neurons *in vivo* (Fig. 1*A*, for details, see Materials and Methods). Injection of three distinct AAVs encoding Cre-dependent fluorescent reporters into the RTN of $Nmb^{Cre/+}$ mice ($n = 6$) resulted in labeling restricted to RTN^{Nmb} neurons (96 ± 2% of labeled neurons contained *Nmb* mRNA), with transduction between 20% and 81% of all RTN^{Nmb} neurons (58 ± 10% of RTN^{Nmb} neurons expressed fluorescent reporter) (Fig. 1*B–D*). To ablate RTN^{Nmb} neurons, we bilaterally microinjected AAV_5-FLEX-Casp3-TEVp in Cre^+ (RTN^{Nmb}-lesion) and Cre^- (control) littermates (Fig. 1*E*). Microinjections in Cre^+ mice eliminated >95% of RTN^{Nmb} neurons while preserving nearby neuronal populations expressing dopamine-β-hydroxylase (*Dbh*) and TH-2 (*Tph2*) (Fig. 1*F–H*). We also observed no difference in DAPI staining or the expression of GFAP at the site of injection (intensity of GFAP in RTN^{Nmb}-lesion vs controls; 0.14 ± 0.02 vs 0.13 ± 0.01 a.u., $n = 3$, Mann–Whitney $U = 4$, $p > 0.99$, Fig. 1*F,G*), showing that the general structure of the RTN was preserved in RTN^{Nmb}-lesion mice. This histologic analysis shows that Casp3-TEVp-mediated cell ablation of RTN^{Nmb} neurons in $Nmb^{Cre/+}$ mice is both effective and highly selective.

Having established a model to selectively eliminate RTN^{Nmb} neurons in adult mice, we first evaluated resting alveolar ventilation by whole-body plethysmography, and examined arterial blood gases and metabolic activity in unrestrained/freely behaving conditions. In RTN^{Nmb}-lesion mice, resting minute-ventilation (V_E) was 31% lower than in control mice (Fig. 1*I*), owing to a lower V_T with no difference in breathing frequency (f_R). The lower V_E resulted in an elevated arterial P_{CO_2} (Pa_{CO_2}) in RTN^{Nmb}-lesion mice (~10 mmHg, Fig. 1*I,J*), while arterial pH was similar between groups, apparently because of the retention of HCO_3^- (i.e., compensated respiratory acidosis, Fig. 1*K,L*). Notably, there was no statistical difference between VCO_2 and VO_2 between RTN^{Nmb}-lesion and control mice during the inactive phase (Fig. 1*M,N*). Alveolar ventilation, calculated using mean values for Pa_{CO_2} and VCO_2, was ~35% lower during quiet breathing in RTN^{Nmb}-lesion mice, which is explained by the reduced V_E. This demonstrates that RTN^{Nmb} neurons are required for optimal alveolar ventilation at rest. Importantly, body weight, body temperature, and locomotor activity were similar between RTN^{Nmb}-lesion mice and controls, and RTN^{Nmb}-lesion mice exhibited normal diurnal patterns in metabolic activity (Table 2), which indicates that these mice were in good physical condition.

Effect of RTN^{Nmb} ablation on breathing during sleep and sleep-wake patterns

The regulation of breathing varies with change in vigilance state, and this has many implications for sleep-related breathing disorders. During NREMS, V_E is mostly maintained by the chemical drive arising from the chemoreceptors; and we therefore suspected that RTN^{Nmb}-lesion would exhibit deficits in V_E mostly during NREMS sleep. For this, we assessed breathing during wakefulness, NREMS and REMS (Fig. 2*A–C*). We observed a significantly lower V_T in RTN^{Nmb}-lesion compared with control, and no interaction between ablation of RTN^{Nmb} neurons and vigilance state, whereas there was no significant difference in f_R regardless of the vigilance state. There was also a significant effect of ablation of RTN^{Nmb} neurons on V_E, and no significant interaction between ablation of RTN^{Nmb} neurons and vigilance state. *Post hoc* analysis indicates that the deficits in V_T and V_E in RTN^{Nmb}-lesion are most evident during NREMS. Collectively, this analysis shows that, in normoxic conditions, ablation of RTN^{Nmb} neurons reduces V_E across all vigilance states, but most profoundly during NREMS.

A more detailed examination of the breathing pattern revealed the presence of a distinctive phenotype in RTN^{Nmb}-lesion mice, namely, a significant increase in the variability of respiratory cycle duration (Fig. 2*D–F*). This was evident when comparing raw flow traces of highly regular breathing pattern in control mice with the more erratic pattern in RTN^{Nmb}-lesion mice (Fig. 2*D*), and a greater dispersion of data points in Poincaré plots (Fig. 2*E*). When compared with control mice by two-way ANOVA, there was a significant increase in breathing variability and no interaction with vigilance state (Fig. 2*F*). Although RTN^{Nmb}-lesion mice had unstable breathing across all vigilance states, this effect was most evident during NREMS, a period typically associated with very stable breathing. During periods of NREMS, RTN^{Nmb}-lesion mice exhibited breathing instability consisting of rapid accelerations in f_R (i.e., tachypneas) followed by hypoventilation (Fig. 2*D*, right) but few apnea events by standard criteria (respiratory pauses longer than 1s). Breathing instability in RTN^{Nmb}-lesion mice was most evident on entry to NREMS (early phase), whereas breathing during periods of NREMS preceding the onset of REMS (late phase) were more stable (Fig. 2*G,H*). We observed a similar relationship between breathing variability and NREMS in control mice (i.e.,

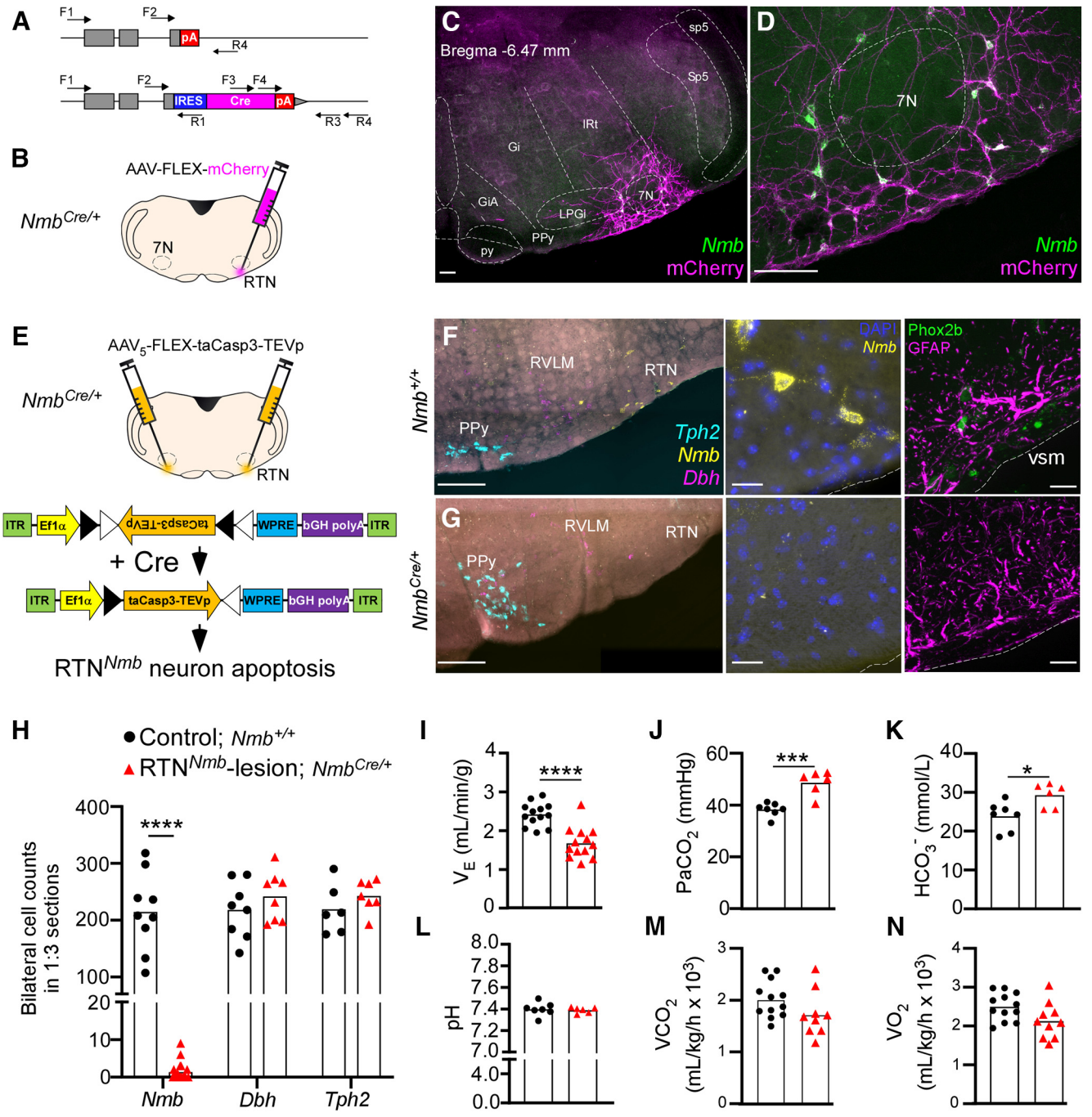

Figure 1. Genetically targeted ablation of Neuromedin B (*Nmb*)-expressing neurons in the RTN produces alveolar hypoventilation. ***A***, Gene targeting of Cre in *Nmb* allele. *Nmb*-Cre mice were generated by homologous recombination, inserting an IRES-Cre-pA cassette at the stop codon in exon 3 of the *Nmb* locus. ***B***, Experimental setup for *in vivo* validation of the *Nmb-Cre* mice. ***C***, Transverse section of mouse medulla showing *Nmb*-expressing RTN neurons (RTN^{Nmb}) labeled with a Cre-dependent mCherry. Viral transduction was confined to the RTN/parafacial region. Note the extensive dendrites at the caudal end of the facial nucleus. ***D***, Same as in ***C***, except at a higher magnification showing *Nmb* transcript in neurons that express mCherry. ***E***, Experimental strategy for genetically targeted ablation of the RTN^{Nmb} neurons with AAV5-FLEX-taCasp3-TEVp. ***F***, ***G***, Coronal sections showing the ventral surface of the medulla of a control mouse in ***F***, and RTN^{Nmb}-lesion mice in ***G***, 6 weeks after injection of AAV_5-FLEX-taCasp3-TEVp. Left panels, FISH for *Nmb*, *Dbh*, and *Tph2*. Note the absence of *Nmb* cells (yellow) in the RTN of RTN^{Nmb}-lesion mice, but similar expression of *Dbh* and *Tph2* in the same section. Middle panels, *Nmb* and DAPI expression at high magnification. DAPI expression at the site of AAV injection was comparable between groups. Right, GFAP expression in marginal glia and Phox2b immunofluorescence. GFAP expression is similar between groups. ***H***, Cell counts in control and RTN^{Nmb}-lesion mice. Unpaired *t* test with Welch's correction *Nmb*: $t = 9.29$, $df = 8$, $p < 0.0001$. *Dbh*: $t = 1.02$, $df = 14$, $p = 0.32$. *Tph2*: $t = 1.13$, $df = 8$, $p = 0.29$. ***I***, Minute ventilation (V_E). Unpaired *t* test, $t = 5.31$, $df = 24$. $p < 0.0001$. ***J***, Arterial P_{CO_2}. Unpaired *t* test, $t = 5.1$, $df = 11$, $p = 0.0003$. ***K***, Arterial blood bicarbonate. Unpaired *t* test, $t = 2.860$, $df = 11$, $p = 0.0155$. ***L***, Arterial blood pH. Unpaired *t* test, $t = 0.3557$, $df = 11$, $p = 0.7288$. ***M***, Metabolic CO_2 production (VCO_2). Unpaired *t* test, $t = 1.00$, $df = 22$. $p = 0.33$. ***N***, Metabolic O_2 consumption (VO_2). Unpaired *t* test, $t = 1.03$, $df = 19$, $p < 0.0001$. $p = 0.31$. 7N, Facial motor nucleus; Gi, gigantocellular reticular nucleus; GiA, gigantocellular reticular nucleus, α part; IRt, intermediate reticular nucleus; LPGi, lateral paragigantocellular nucleus; RVLM, rostral ventrolateral medulla; Sp5, spinal trigeminal nucleus; sp5; spinal trigeminal tract; vsm, ventral surface of medulla. Scale bars: ***C***, ***D***, 250 μm; ***F***, ***G***, left to right, 250, 5, and 100 μm, respectively.

Table 2. Body weight, body temperature, locomotor activity, and VCO_2 and VO_2 in control and RTN^{Nmb}-lesion mice

	Control	RTN^{Nmb}-lesion	*t*, df	*p* value (*t* test)
Body weight (g)	23.8 ± 3 (*n* = 17)	24.0 ± 3 (*n* = 17)	0.17, 32	0.8635
Body temperature (°C)	37.0 ± 0.3 (*n* = 7)	37.1 ± 0.6 (*n* = 7)	0.59, 12	0.5671
Locomotor activity (a.u.)	0.8 ± 0.04 (*n* = 17)	0.8 ± 0.04 (*n* = 16)	0.14, 31	0.8903
				p (ANOVA)
VCO_2 (ml/kg/h)	*n* = 17	*n* = 14	$F_{(1,29)} = 1.49$	0.2311
Light	1965 ± 351	1832 ± 408	—	—
Dark	3349 ± 547	3006 ± 662	—	—
VO_2 (ml/kg/h)	*n* = 17	*n* = 14	$F_{(1,29)} = 0.94$	0.3383
Light	2432 ± 353	2254 ± 442	—	—
Dark	3568 ± 567	3246 ± 658	—	—

higher variability during early phase NREMS), but variability was always higher in RTN^{Nmb}-lesion mice. The instability of breathing during early phase NREMS is presumably the effects of the rapid withdrawal of the waking drive to breathe (Dempsey, 2019).

Owing to the severity of respiratory dysfunction in RTN^{Nmb}-lesion mice during NREMS, we sought to determine whether ablation of RTN^{Nmb} neurons influences sleep-wake patterns based on a 4 h recording period in normoxic conditions beginning between 1000 and 1200 h (Fig. 3). Based on blinded scoring of vigilance state in 20 s epochs independent of breathing pattern, RTN^{Nmb}-lesion mice spent the same amount of time in both NREMS and REMS as control mice and had comparable slow-wave activity (δ power) during NREMS (Fig. 3*A*–*C*). Furthermore, while oscillatory breathing during NREMS in RTN^{Nmb}-lesion mice was occasionally associated with instances of cortical desynchronizations (<1 s), those breathing patterns generally occurred without a detectable change in EEG activity (Fig. 2*D*, right). However, we did observe a significant increase in the incidence of microarousals during NREMS sleep (EEG desynchronization <10 s) (Fig. 3*D*–*G*). When aligned with breathing patterns, these microarousals were always associated with respiratory-related events and commonly with sighs (Fig. 3*E*–*G*). Collectively, these data show that a loss of RTN^{Nmb} neurons causes hypoventilation and breathing instability and increases respiratory-related sleep disturbances (micro-arousals) without disrupting general sleep-wake processes.

Effect of hyperoxia on breathing stability

In addition to increased Pa_{CO_2}, we found a significant reduction in arterial P_{O_2} (Pa_{O_2}) in RTN^{Nmb}-lesion mice, with 5 of 6 mice having values <80 mmHg during periods of unrestrained quiet breathing. This characterizes a state of chronic hypoxemia (Fig. 4*A*) sufficient to activate the peripheral chemoreceptors (Lopez-Barneo, 2022). Thus, we hypothesized that hypoxic drive may be an important compensatory mechanism that supports breathing in the absence of RTN^{Nmb} neurons. To test this, we exposed mice to hyperoxia ($F_IO_2 = 0.60$) to relieve the hypoxemia in RTN^{Nmb}-lesion mice. Hyperoxia produced an immediate and profound hypoventilation in RTN^{Nmb}-lesion mice, whereas it had negligible effects on breathing in controls (Fig. 4*B*–*D*). In addition to a reduction in f_R, hyperoxia in RTN^{Nmb}-lesion mice markedly increased breathing variability (Fig. 4*E*) and led to the appearance of apneas (expiratory duration >1 s, Fig. 4*F*). Furthermore, RTN^{Nmb}-lesion mice exhibited a greater sigh frequency in normoxic conditions relative to controls, and this was normalized during periods of hyperoxia (Fig. 4*G*,*H*), suggesting that effects related to hypoxemia following ablation of RTN^{Nmb} neurons underlies this enhanced sigh frequency. We also noted that the inspired volume during sighs was significantly larger in RTN^{Nmb}-lesion mice compared with controls, but this was not corrected by hyperoxia (Fig. 4*I*). Collectively, these experiments demonstrate that O_2-sensitive mechanisms compensate for the loss of respiratory drive following ablation of RTN^{Nmb} neurons.

Hypercapnic ventilatory responses

Consistent with the molecular phenotype of *Nmb*-expressing neurons in the RTN (i.e., expression of specific molecular proton detectors implicated in CO_2/H^+ sensing, TASK2 and GPR4), we hypothesize that RTN^{Nmb} neurons mediate the respiratory response to central chemoreflex activation by CO_2. To test this hypothesis, we first examined the effect of hypercapnia in hyperoxic conditions to isolate the central component of the HCVR. Under these conditions, hypercapnia produced a very small increase in the f_R, V_T, and V_E in RTN^{Nmb}-lesion mice (Fig. 5*A*–*D*), reducing the ΔV_E in response to 9% CO_2 from an increase of 9.65 ± 0.74 ml/min/kg in intact mice to only 1.89 ± 0.34 ml/min/kg in RTN^{Nmb}-lesion mice (control vs RTN^{Nmb}-lesion; unpaired *t* test, $t = 9.284$, df = 29, $n = 16$ and 15, $p < 0.0001$). Interestingly, ΔV_E during hypercapnia in RTN^{Nmb}-lesion mice was similar in normoxic and hyperoxic conditions (Fig. 5*E*). According to linear regression of V_E during hypercapnia (mean $R^2 = 0.80 \pm 0.03$), the sensitivity of HCVR in RTN^{Nmb}-lesion mice was reduced by 94% in normoxic conditions and 86% in hyperoxic conditions compared with control mice (Fig. 5*F*). Notably, despite a large reduction in the HCVR in RTN^{Nmb}-lesion mice compared with controls, there was still a significant residual increase in V_E from baseline during hypercapnia by one-way ANOVA (Fig. 5*E*). In addition to deficits in the HCVR, we also found that stabilizing effect of hypercapnia on breathing frequency observed in controls was absent in RTN^{Nmb}-lesion mice (Fig. 5*G*). That is, whereas breathing variability decreased between 0% and 9% CO_2 in control mice, it was higher in RTN^{Nmb}-lesion mice and did not change across that range of CO_2 (Fig. 5*H*). In sum, the ablation of RTN^{Nmb} neurons in adult mice essentially eliminates the HCVR and disrupts the stabilizing effects of hypercapnia on breathing.

Hypoxic ventilatory responses

Given the dramatic attenuation in the HCVR of RTN^{Nmb}-lesion mice, we examined the possibility that ablation of RTN neurons reduces the sensitivity of the respiratory central pattern generator to other stimulants of breathing. To this end, we examined the hypoxic ventilatory response, which is understood to be mediated primarily by the peripheral chemoreceptors (Lopez-Barneo, 2022). In contrast to the effect of hypercapnia in RTN^{Nmb}-lesion mice, the increase in V_E during graded hypoxia was not attenuated in RTN^{Nmb}-lesion after accounting for baseline differences (Fig. 6*A*–*E*). Indeed, there was a notable sensitization of the f_R response and an attenuated V_T response to hypoxia in RTN^{Nmb}-lesion mice (Fig. 6*B*,*C*). Furthermore, unlike the effects of hypercapnia noted above, hypoxia stabilized breathing patterns in RTN^{Nmb}-lesion mice (Fig. 6*F*,*G*). This suggests that breathing instability in RTN^{Nmb}-lesion mice is likely caused by deficits that are specific to the CO_2-mediated drive to breathe. Unstable breathing during the post-hypoxia recovery period is a well-known characteristic of mice (Yamauchi et al., 2007; Getsy et al., 2014) that was present in both controls and RTN^{Nmb}-lesion mice

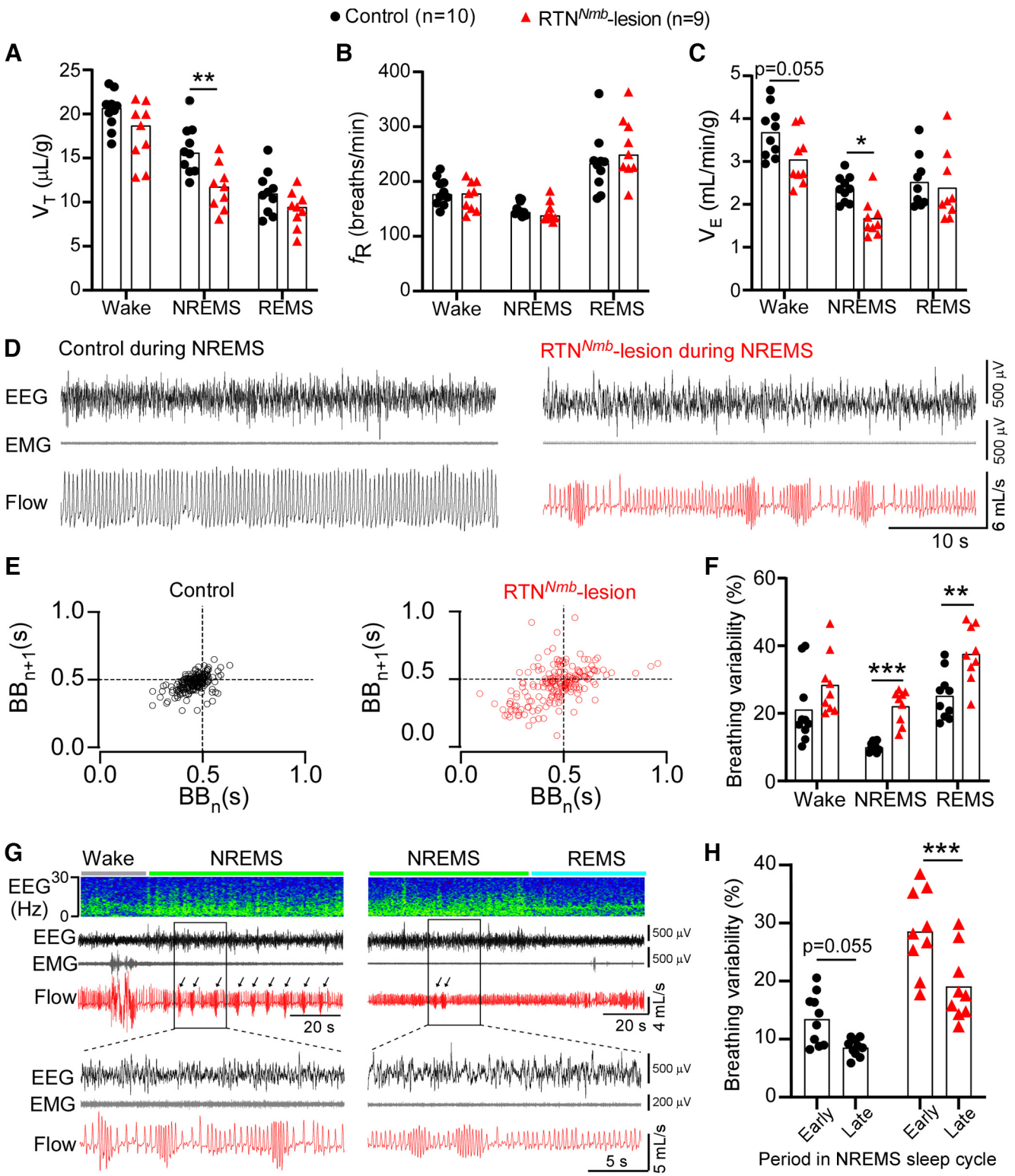

Figure 2. Complete RTN^{Nmb}-lesion produces hypoventilation and breathing instability. ***A***, Effects of RTN^{Nmb}-lesion on V_T across vigilance states. Two-way repeated-measures ANOVA, RTN-lesion versus state; interaction, $F_{(2,34)} = 3.17$, $p = 0.054$. State, $F_{(2,29)} = 176.6$, $p < 0.0001$. Lesion, $F_{(1,17)} = 7.5$, $p = 0.014$. ***B***, Effects of RTN^{Nmb}-lesion on f_R across vigilance states. Two-way repeated-measures ANOVA, RTN^{Nmb}-lesion versus state; interaction, $F_{(2,34)} = 2.06$, $p = 0.14$. State, $F_{(2,34)} = 55.9$, $p < 0.0001$. Lesion, $F_{(1,17)} = 0.13$, $p = 0.72$. ***C***, Effects of RTN^{Nmb}-lesion on V_E across vigilance states. Two-way repeated-measures ANOVA, RTN^{Nmb}-lesion versus state; interaction, $F_{(2,34)} = 3.2$, $p = 0.051$. State, $F_{(2,34)} = 65.8$, $p < 0.0001$. Lesion, $F_{(1,17)} = 4.7$, $p = 0.044$. ***D***, Representative recordings of EEG and breathing patterns (Flow) during NREM sleep in control and RTN^{Nmb}-lesion mice. Note periods of tachypnea followed by hypoventilation that occur in bouts. ***E***, Representative Poincaré plots showing the breath duration (BB_n) in relation to the subsequent breath duration (BB_{n+1}) in control and RTN^{Nmb}-lesion mice. ***F***, Effects of RTN^{Nmb}-lesion on breathing variability across vigilance states. Two-way repeated-measures ANOVA, RTN^{Nmb}-lesion versus state; interaction, $F_{(2,34)} = 0.86$, $p = 0.4310$. State, $F_{(2,30)} = 24.4$, $p < 0.0001$. Lesion, $F_{(1,17)} = 21.4$, $p = 0.0002$. ***G***, Representative recordings of breathing patterns during entry to sleep after a period of continuous waking (>10 min in this case) defined as early NREMS, and later in the same recording immediately before the onset of a REMS period defined as late NREMS. Arrows indicate periods of oscillatory breathing, which occur more frequently during early NREMs than late NREMS. ***H***, Breathing variability during early NREMS and late NREMS in control and RTN^{Nmb}-lesion mice. Two-way repeated-measures ANOVA, RTN^{Nmb}-lesion versus time in NREMS cycle; interaction, $F_{(1,17)} = 2.35$, $p = 0.14$. State, $F_{(1,17)} = 23.5$, $p = 0.0002$. Lesion, $F_{(1,17)} = 48.1$, $p < 0.0001$. *$p < 0.05$; **$p < 0.01$; ***$p < 0.001$; Control versus RTN^{Nmb}-lesion mice by Bonferroni's multiple comparisons (***A-H***).

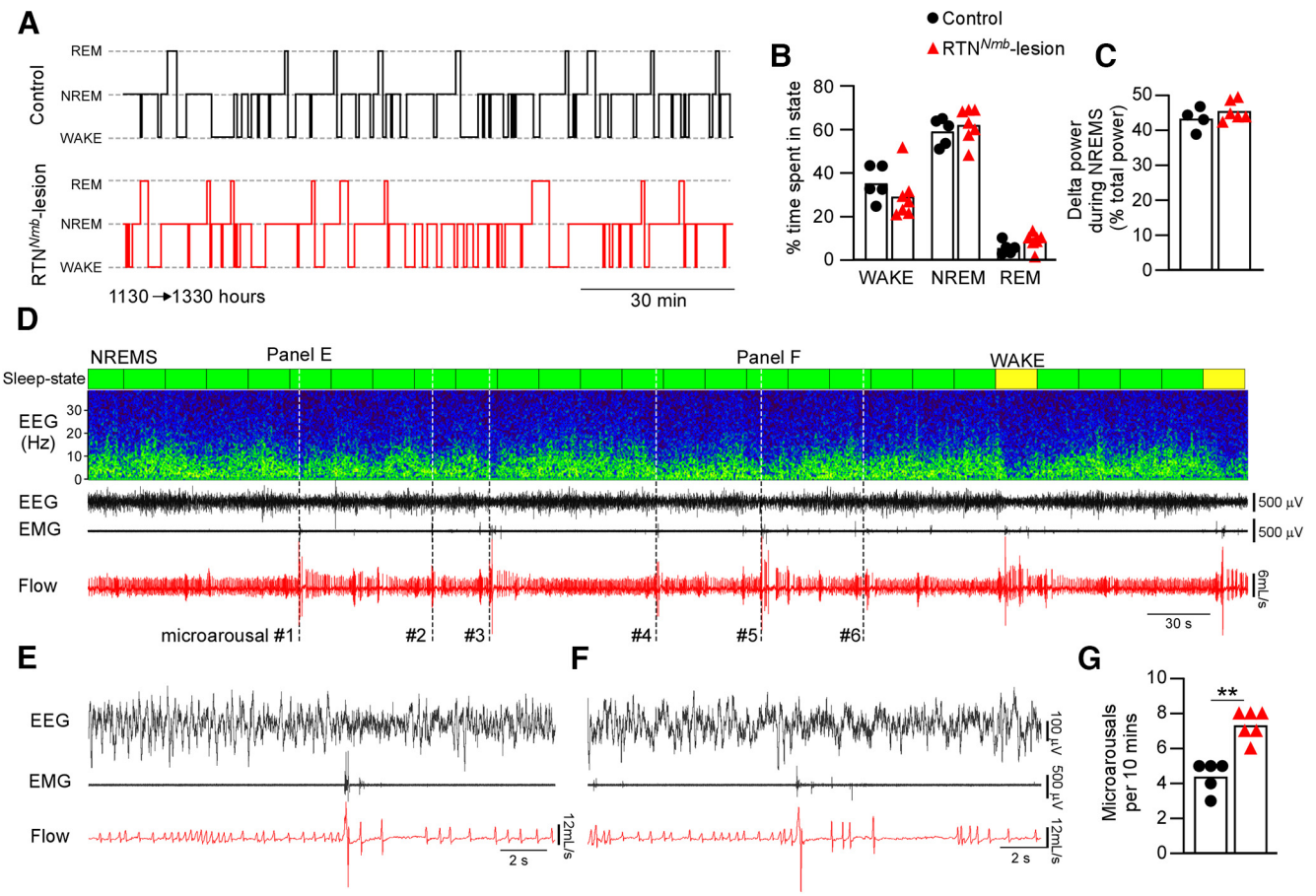

Figure 3. RTN^{Nmb}-lesion does not reduce the total time spent in NREMS sleep but increases respiratory-related microarousals. ***A***, Hypnogram of sleep-wake patterns during a single plethysmography recording session. ***B***, Percent time spent in each vigilance state over a 4 h recording period in control and RTN^{Nmb}-lesion mice. Two-way ANOVA, RTN^{Nmb}-lesion versus state; interaction, $F_{(2,30)} = 1.54$, $p = 0.23$. State, $F_{(2,30)} = 157.7$, $p < 0.0001$. Lesion, $F_{(1,30)} = 2.9e^{-17}$, $p > 0.99$. ***C***, Total power in δ band (0.5-4.5 Hz) of FFT power spectrum of EEG during NREMS in Control and RTN^{Nmb}-lesion mice. Mann–Whitney test, $U = 8$. $p = 0.48$. ***D***, Representative recording of sleep-wake state scoring using a 20 s window, EEG (moving power-spectrum and raw signal) neck EMG and breathing patterns (Flow) in a RTN^{Nmb}-lesion mouse. There was an increase in microarousals (<10 s of cortical desynchronization), consisting of coincident activation of breathing, EEG, and EMG in RTN^{Nmb}-lesion mice. ***E***, ***F***, Expanded examples from ***D***. ***G***, Microarousals per 10 min of NREMS in control and RTN^{Nmb}-lesion mice. Control versus RTN^{Nmb}-lesion mice. Mann–Whitney test, $U = 0$. $p = 0.004$.

(Fig. 6*H*). It has been suggested that unstable breathing in this condition is mostly related to hypocapnia/alkalosis that occurs with hypoxia-induced increases in V_E (Yamauchi et al., 2007). Collectively, these data show that the hypoxic ventilatory response does not require RTN^{Nmb} neurons and that the respiratory central pattern generator is functionally intact in RTN^{Nmb}-lesion mice. However, there appears to be a reorganization of the hypoxic ventilatory response that promotes tachypnea to compensate for an inadequate recruitment of V_T during hypoxia. Also, the persistence of unstable breathing during the post-hypoxia period in RTN^{Nmb}-lesion mice suggests that this effect is not only due the effects of hypocapnia/alkalosis on RTN^{Nmb} neurons.

Optogenetic inhibition of RTN^{Nmb} neurons

Our experiments using bilateral ablation of RTN^{Nmb} neurons indicate that these neurons contribute at least one-third of the drive to breathe during resting V_E. However, as demonstrated by the effects of hyperoxia, there is likely a degree of physiological compensation that occurs following ablation that could result in an underestimation of the contribution of RTN^{Nmb} neurons to resting V_E. Hence, we performed acute and reversible optogenetic inhibition of RTN^{Nmb} neurons using the inhibitory proton pump eArch3.0 to assess the instantaneous contribution of these neurons to V_E (Fig. 7). To improve the efficacy of our approach, RTN^{Nmb} neurons were ablated in the right RTN using AAV$_5$-FLEX-Casp3-TEVp, and a unilateral optical fiber was used to illuminate (and inhibit) the remaining contralateral RTN^{Nmb} neurons expressing eArch3.0 (selectivity: 98.9 ± 1.1%; coverage: 58.3 ± 11.5% $n = 3$) (Fig. 7*A–C*). Notably, the HCVR of mice with unilateral ablation of RTN^{Nmb} neurons was similar to controls (compare Fig. 7*J* with Fig. 5*D*), consistent with our work in rats demonstrating that deficits in respiratory control are only observable after nearly all of the RTN^{Nmb} neurons are eliminated (Souza et al., 2018).

Unilateral opto-inhibition of RTN^{Nmb} neurons resulted in an immediate reduction in V_E in all vigilance states (Fig. 7*D–H*). Inhibition of RTN^{Nmb} neurons caused a comparable reduction in f_R, V_T, and V_E during both waking and NREMS, whereas the effects on f_R and V_T were less pronounced and more variable during REMS, similar to previous studies in rats (Burke et al., 2015), which confirms a diminished significance for RTN^{Nmb} neurons in the control of breathing during this state. Complete apnea was not observed during optogenetic inhibition of RTN^{Nmb} neurons in normoxic conditions. However, hyperoxia enhanced the effect of opto-inhibition (ΔV_E during RTN^{Nmb} neuron inhibition in normoxic vs hyperoxic; −1.61 ± 0.20 vs −2.37 ± 0.31 ml/min/kg, $n = 5$, paired t test $t = 4.141$, df = 4,

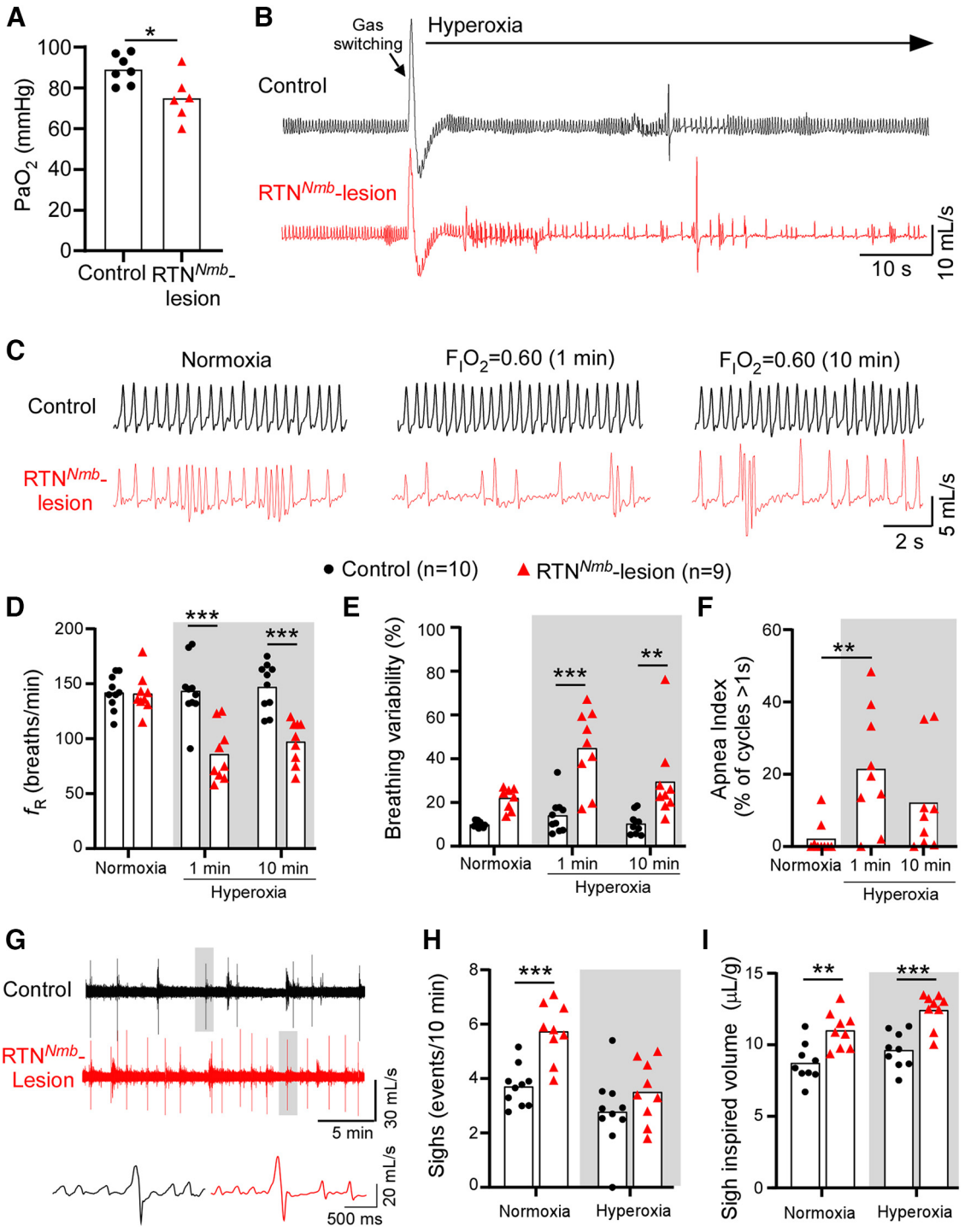

Figure 4. Breathing is driven by hypoxia in RTN^{Nmb}-lesion mice. ***A***, Pa_{O_2} in control ($n = 7$) and RTN^{Nmb} -lesion mice ($n = 6$) in normoxic, resting conditions. Unpaired *t* test, $t = 2.757$, df = 1, $p = 0.0186$. *$p < 0.01$ (*t* test). ***B***, Breathing responses to acute hyperoxia ($F_IO_2 = 0.6$) in control ($n = 10$) and RTN^{Nmb}-lesion ($n = 9$). RTN^{Nmb}-lesion mice present a more pronounced reduction in f_R in response to hyperoxia compared with control. ***C***, Breathing in response to hyperoxia 1 min (middle) and 10 min (right) after the beginning of the stimulus. Hyperoxia exacerbates breathing variability in RTN^{Nmb}-lesion mice but not in control mice. Hyperoxia also promotes apnea (pauses in respiratory cycle longer than 1 s). Control mice presented no apnea in response to hyperoxia. ***D***, f_R. Two-way repeated-measures ANOVA, RTN^{Nmb}-lesion versus hyperoxia; interaction, $F_{(2,34)} = 14.2$, $p < 0.0001$. Hyperoxia, $F_{(2,34)} = 11.5$, $p = 0.0002$. Lesion $F_{(1,17)} = 24.5$, $p = 0.0001$. ***E***, Breathing variability. Two-way repeated-measures ANOVA, RTN^{Nmb}-lesion versus hyperoxia; interaction, $F_{(1,34)} = 4.3$, $p = 0.0218$. Hyperoxia, $F_{(2,34)} = 9.3$, $p = 0.0006$. Lesion, $F_{(1,17)} = 33.6$, $p < 0.0001$. ***F***, Apnea index. Friedman's test; $p = 0.0024$. **$p < 0.01$ (Dunn's multiple comparisons). ***G***, Sigh events in control and RTN^{Nmb}-lesion mice. The frequency of the sighs is increased in RTN^{Nmb}-lesion mice and the V_T increased. ***H***, Sigh frequency. Two-way repeated-measures ANOVA, RTN^{Nmb}-lesion versus hyperoxia; interaction, $F_{(1,17)} = 6.3$, $p = 0.0223$. Hyperoxia, $F_{(1,17)} = 37.2$, $p < 0.0001$. Lesion, $F_{(1,34)} = 10.2$, $p = 0.0053$. ***I***, Sigh inspired volume. Two-way repeated-measures ANOVA, RTN^{Nmb}-lesion versus hyperoxia; interaction, $F_{(1,16)} = 0.89$, $p = 0.3571$. Hyperoxia, $F_{(1,16)} = 17.2$, $p = 0.0008$. Lesion, $F_{(1,16)} = 22.9$, $p = 0.0002$. **$p < 0.01$, ***$p < 0.001$ versus controls by Bonferroni's multiple comparisons test in ***D-I***.

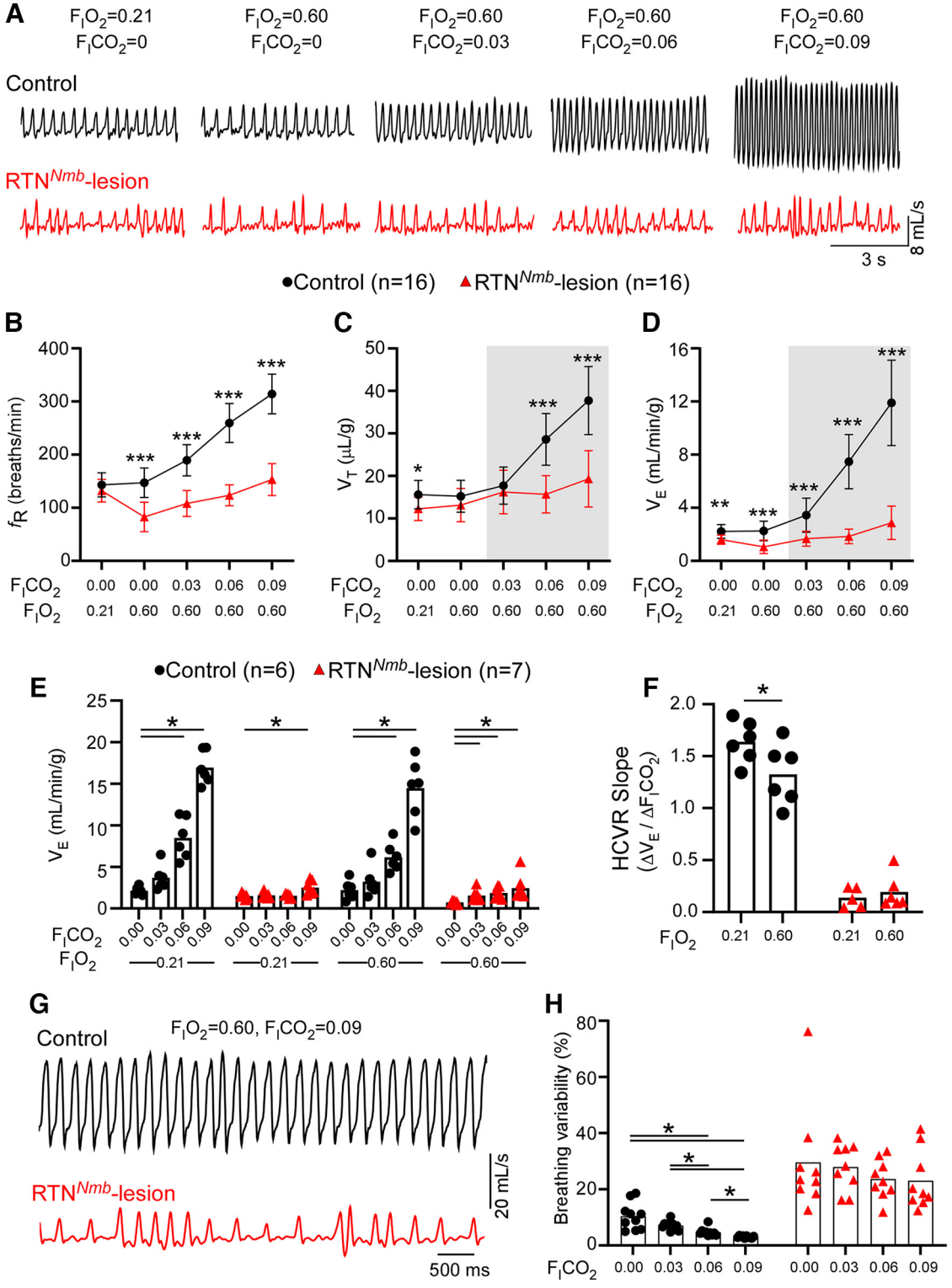

Figure 5. RTN^{Nmb}-lesion attenuates the HCVR and the effects of CO_2 on breathing variability. ***A***, Representative recordings of breathing during hypercapnia in controls and RTN^{Nmb}-lesion mice. Only controls exhibit a graded increase in V_E as F_ICO_2 increases. ***B***, Effects of RTN^{Nmb}-lesion on f_R during hypercapnia. Two-way repeated-measures ANOVA, RTN-lesion versus CO_2 condition; interaction, $F_{(4,120)} = 74.2$, $p < 0.0001$. CO_2 condition, $F_{(3,96)} = 188.5$, $p < 0.0001$. Lesion, $F_{(1,30)} = 132.3$, $p < 0.0001$. ***C***, Effects of RTN^{Nmb}-lesion on V_T during hypercapnia. Two-way repeated-measures ANOVA, RTN-lesion versus CO_2 condition; interaction, $F_{(4,120)} = 29.5$, $p < 0.0001$. CO_2 condition, $F_{(3,85)} = 78.3$, $p < 0.0001$. Lesion, $F_{(1,30)} = 35.2$, $p < 0.0001$. ***D***, Effects of RTN^{Nmb}-lesion on V_E during hypercapnia. Two-way repeated-measures ANOVA, RTN-lesion versus CO_2 condition; interaction, $F_{(4,120)} = 70$, $p < 0.0001$. CO_2, $F_{(2,54)} = 126.1$, $p < 0.0001$. Lesion, $F_{(1,30)} = 135.7$, $p < 0.0001$. ***E***, Comparison of the HCVR in RTN^{Nmb}-lesion and control mice in normoxia and hyperoxia. One-way repeated-measures ANOVA. Controls in normoxia; $F_{(2,8)} = 73.15$, $p < 0.0001$. RTN^{Nmb}-lesion in normoxia; $F_{(1,7)} = 6.697$, $p = 0.036$. Controls in hyperoxia; $F_{(2,9)} = 79.77$, $p < 0.0001$. RTN^{Nmb}-lesion in hyperoxia; $F_{(2,9)} = 5.822$, $p = 0.028$. ***F***, Slope of linear regression for HCVR data in ***E***. Two-way ANOVA, RTN^{Nmb} -lesion versus O_2 condition; interaction, $F_{(1,19)} = 4.699$, $p = 0.0431$. O_2 condition, $F_{(1,19)} = 2.278$, $p = 0.148$, $p < 0.0001$. Lesion, $F_{(1,19)} = 237.1$, $p < 0.0001$. ***G***, Breathing recordings during hypercapnia in controls and RTN^{Nmb}-lesion mice. Note variability present in RTN^{Nmb}-lesion mice even under high CO_2. ***H***, Effects of RTN^{Nmb}-lesion on the breathing variability during hypercapnia. One-way repeated-measures ANOVA. Controls; $F_{(1.312,\ 11.81)} = 17.08$, $p = 0.0008$. RTN^{Nmb}-lesion; $F_{(2,13)} = 1.249$, $p = 0.31$. *$p < 0.05$, **$p < 0.01$, ***$p < 0.001$ versus controls by Bonferroni's multiple comparisons test in ***B-D***, ***F***, versus baseline by Holm–Sidak's multiple comparisons test for ***E***, versus other CO_2 conditions by Tukey's multiple comparisons for ***H***.

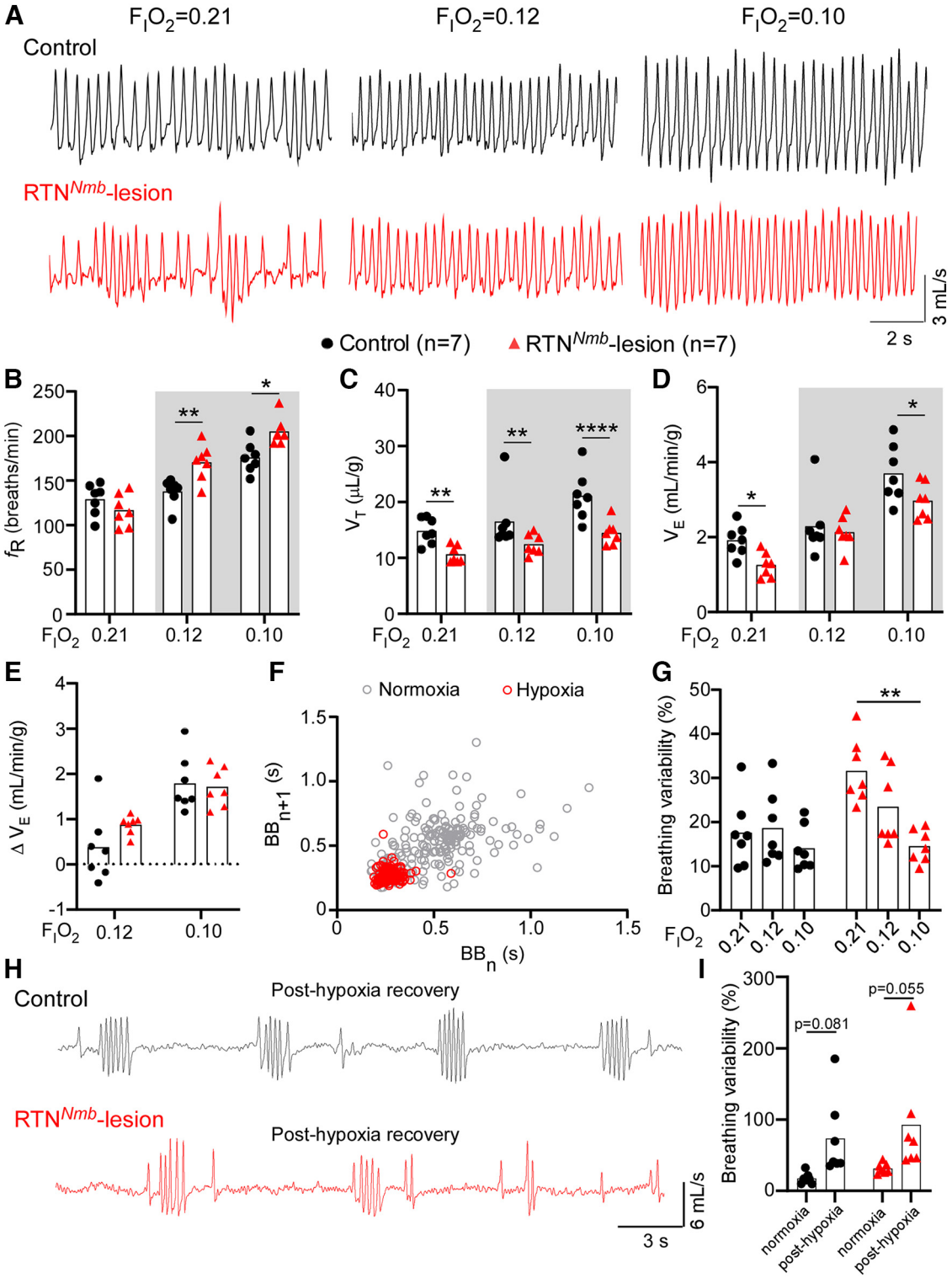

Figure 6. RTN^{Nmb}-lesion does not attenuate the hypoxic ventilatory response or the effects of hypoxia on breathing variability. ***A***, Breathing recordings from control and RTN^{Nmb}-lesion mice during hypoxia (F_IO_2 = 0.12 and 0.1). Hypoxia increases ventilation and reduces the breathing variability in both control and RTN^{Nmb}-lesion mice. ***B***, Effects of RTN^{Nmb}-lesion on f_R during hypoxia. Two-way repeated-measures ANOVA, RTN-lesion versus O_2 condition; interaction, $F_{(2,24)} = 10.2$, $p = 0.0006$. O_2 condition, $F_{(2,24)} = 75.3$, $p < 0.0001$. Lesion, $F_{(1,12)} = 6.1$, $p = 0.0299$. ***C***, Effects of RTN^{Nmb}-lesion on V_T during hypoxia. Two-way repeated-measures ANOVA, RTN-lesion versus O_2 condition; Interaction, $F_{(2,24)} = 2.1$, $p = 0.1368$. O_2 condition, $F_{(2,24)} = 27.2$, $p < 0.0001$. Lesion effect $F_{(1,12)} = 10.7$, $p = 0.0066$. ***D***, Effects of RTN^{Nmb}-lesion on V_E during hypoxia. Two-way repeated-measures ANOVA, RTN-lesion versus O_2 condition; interaction, $F_{(2,24)} = 1.9$, $p = 0.1692$. O_2 condition, $F_{(2,24)} = 62.9$, $p < 0.0001$. Lesion, $F_{(1,12)} = 4.4$, $p = 0.0556$. ***E***, Changes in V_E from baseline. Two-way repeated-measures ANOVA, RTN-lesion versus O_2 condition; interaction, $F_{(1,12)} = 2.5$, $p = 0.1365$. O_2 condition, $F_{(1,12)} = 39.6$, $p < 0.0001$. Lesion, $F_{(1,12)} = 0.81$, $p = 0.3854$. ***F***, Poincaré plots of breath-to-breath interval (BB_n) and subsequent breath-to-breath interval (BB_{n+1}) from an RTN^{Nmb}-lesion mouse in normoxia and during hypoxia (F_IO_2 = 0.1). Breathing becomes less variable during hypoxia. ***G***, Breathing variability during hypoxia. One-way repeated-measures ANOVA. Control, $F_{(2,9)} = 1.2$, $p = 0.3325$; RTN^{Nmb}-lesion, $F_{(2,12)} = 15.6$, $p = 0.0006$. $^{**}p < 0.01$ from Tukey's multiple comparisons. ***H***, Breathing recordings during the reoxygenation period following hypoxia. Recordings taken 1-2 min after switching the gas condition from hypoxia (F_IO_2 = 0.1) to normoxia. Reoxygenation following hypoxia increases variability of breathing in both control and RTN lesion mice. ***I***, Breathing variability during reoxygenation in control and RTN^{Nmb}-lesion mice. Two-way repeated-measures ANOVA, RTN^{Nmb}-lesion versus O_2 condition; interaction, $F_{(1,12)} = 0.02270$, $p = 0.88$. O_2 condition, $F_{(1,12)} = 11.43$, $p = 0.006$. Lesion, $F_{(1,12)} = 0.7796$, $p = 0.40$. $^{*}p < 0.05$, $^{**}p < 0.01$, $^{***}p < 0.001$ versus controls by Bonferroni's multiple comparisons test in ***B-D***, and by Holm–Sidak's multiple comparisons test for ***G***.

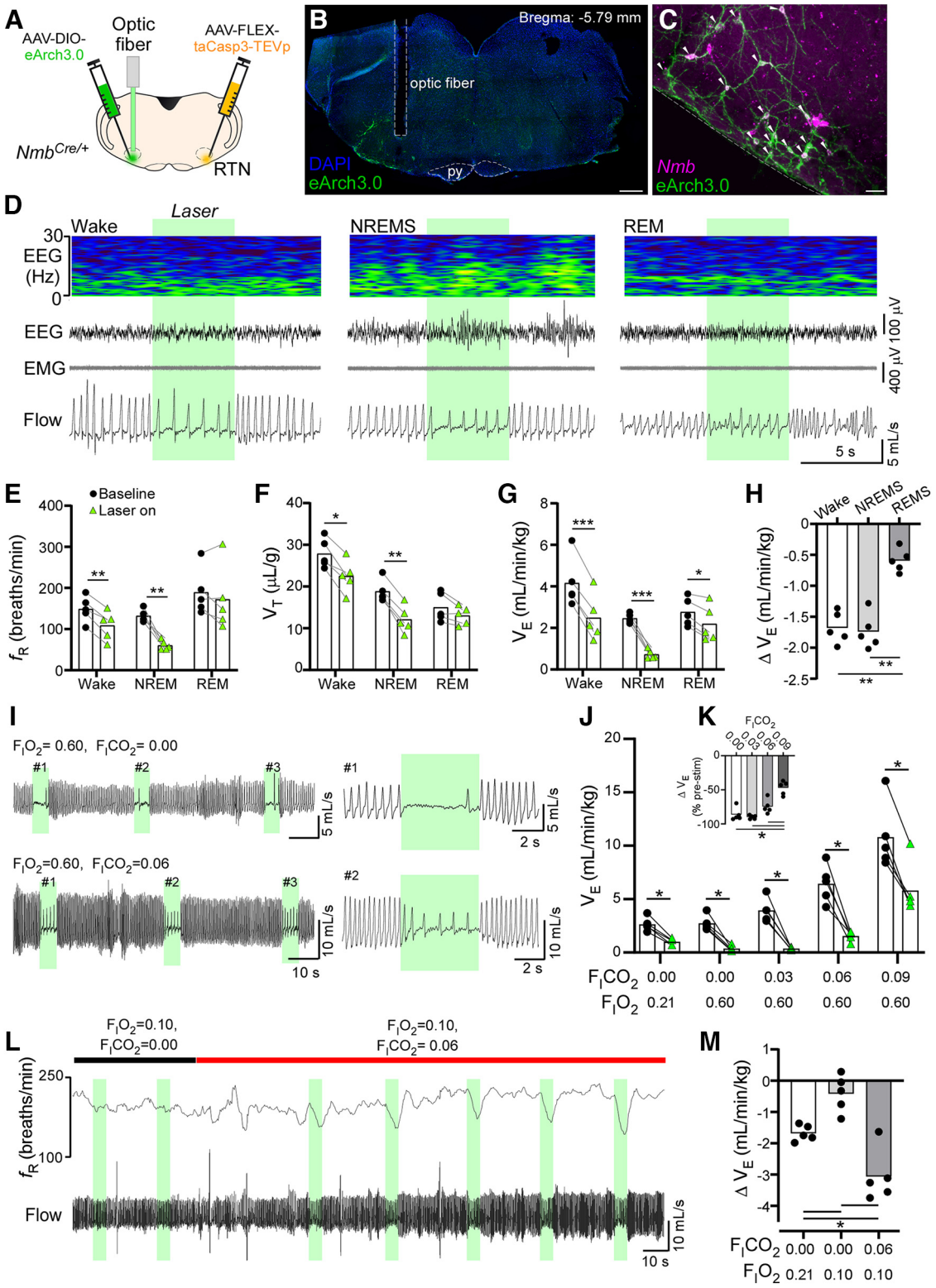

Figure 7. Acute optogenetic inhibition of RTN^{Nmb} neurons produces hypoventilation. ***A***, Experimental setup for the optogenetic inhibition of RTN^{Nmb} neurons. ***B***, Photomicrograph showing the optical fiber tract and RTN^{Nmb} neurons transduced with eArch3.0. Scale bar, 400 µm ***C***, ISH showing *Nmb* neurons expressing eArch3.0-eYFP. Arrowheads indicate double-labeled cells. Scale bar, 100 µm. ***D***, Optogenetic inhibition of RTN^{Nmb} neurons during different stages of the sleep-wake cycle. ***E***, Effect of RTN^{Nmb} neuron inhibition on f_R ($n = 5$). Two-way repeated-measures ANOVA, laser-on versus vigilance state; interaction, $F_{(1,5)} = 5.1$, $p = 0.0754$. Laser-on, $F_{(1,5)} = 5.1$, $p = 0.0754$. vigilance state, $F_{(1,6)} = 6.6$, $p = 0.0402$. ***F***, Effect of RTN^{Nmb} neuron inhibition on V_T. Two-way repeated-measures ANOVA, laser-on versus vigilance state; interaction, $F_{(1,5)} = 5.1$, $p = 0.0754$. Laser-on, $F_{(1,4)} = 659.0$, $p < 0.0001$. Vigilance state, $F_{(1,6)} = 6.6$, $p = 0.0402$. ***G***, Effect of RTN^{Nmb} neuron inhibition on V_E. Two-way repeated-measures ANOVA, laser-on × vigilance state; interaction, $F_{(2,6)} = 28.9$, $p = 0.0009$. Laser-on, $F_{(1,4)} = 526.1$, $p < 0.0001$. Vigilance state, $F_{(2,6)} = 7.4$, $p = 0.0267$. ***H***, ΔV_E during RTN^{Nmb} neuron inhibition. One-way repeated-measures ANOVA, $F_{(2,6)} = 30.1$, $p = 0.0008$. ***I***, Effect of inhibition of RTN^{Nmb} neurons during hyperoxia (top panels) and hyperoxic hypercapnia (bottom panels). The effect of RTN^{Nmb} neuron inhibition during hyperoxia and hyperoxic hypercapnia is increased compared with normoxia. ***J***, Effect of RTN^{Nmb} neuron inhibition on V_E during normoxia, hyperoxia, and hyperoxic hypercapnia. Normoxia versus hyperoxia at 0% CO_2, two-way repeated-measures ANOVA, laser-on versus O_2 condition; interaction, $F_{(1,4)} = 17.14$, $p = 0.0144$. Laser-on, $F_{(1,4)} = 66.38$, $p = 0.0012$. O_2 condition, $F_{(1,4)} = 5.955$, $p = 0.0712$. Effect across CO_2 conditions,

$p = 0.0144$) and produced complete apnea in most trials (Fig. 7*I*, top). In hyperoxic conditions, the effect size of opto-inhibition of RTN^{Nmb} neurons on V_E was also enhanced with graded hypercapnia (Fig. 7*I*,*J*), although the reduction in V_E as a proportion of baseline ventilation was significantly reduced during 9% CO_2 compared with other levels of CO_2 (Fig. 7*K*). Finally, 10% hypoxia essentially eliminated the reduction in V_E during opto-inhibition of RTN^{Nmb} neurons, and this could be reversed by the addition of 6% CO_2 (Fig. 7*L*,*M*). Collectively, this experiment indicates that RTN^{Nmb} neurons provide CO_2/pH-dependent drive to breath that is necessary for optimal V_E across vigilance states. Furthermore, resting eupneic ventilation in hyperoxic conditions is determined by RTN^{Nmb} neurons.

RTN^{Nmb} neuron ablation does not perturb CO_2 avoidance behavior

In mice, hypercapnia produces anxiety-related behaviors and avoidance that has been linked to the detection CO_2 or H^+ by cells in the hypothalamus and limbic system (Ziemann et al., 2009; Vollmer et al., 2016; Taugher et al., 2020). Phox2b-expressing RTN neurons are reported to contribute to arousal from sleep in response to CO_2 in rats and anatomic evidence indicates Phox2b-expressing RTN neurons innervate the LPB, a region involved in aversive behaviors (Abbott and Souza, 2021). Based on this, we tested the hypothesis that RTN neurons contribute to the behavioral response of mice to hypercapnia. We first examined freezing behavior during exposure to CO_2 in an open-field assay. During exposure to 10% CO_2, RTN^{Nmb}-lesion and control mice exhibited freezing for a comparable period of time and had a similar incidence of jumping in both normoxia and hypercapnia (Fig. 8*A*–*C*). Next, we determined whether ablation of RTN^{Nmb} neurons influenced the natural preference of mice for low CO_2 environments using a two-chamber placed-preference assay. Based on a two-way repeated-measures ANOVA, ablation of RTN^{Nmb} neurons did not markedly affect CO_2 avoidance in this assay (Fig. 8*D*,*E*). Collectively, these data suggest that RTN^{Nmb} neurons are not required for freezing, jumping, or avoidance behaviors in response to a high CO_2 environment.

Efferent projections of RTN^{Nmb} neurons

The axonal projections of Phox2b-expressing RTN neurons, a population of neurons that overlaps with but may not be strictly identical to the *Nmb*-expressing RTN neurons, have been well described in rats (Abbott et al., 2011; Silva et al., 2016; Souza et al., 2020) but not in mice. Based on the functional effects of ablating RTN^{Nmb} neurons and known projections of Phox2b-expressing RTN neurons in rats, we hypothesized that RTN^{Nmb} neurons would innervate respiratory-related regions in the pons and medulla. To map the downstream connections of RTN^{Nmb} neurons in mice, we performed genetically targeted efferent tracing experiments. Microinjections of a Cre-dependent AAV-expressing red fluorescent protein (mScarlet) in the RTN labeled a majority of *Nmb*-expressing neurons with high selectivity (selectivity: 98.8 ± 1.2%, coverage: 58.3 ± 11.5% $n = 3$, Fig. 9*C*,*D*). In these cases, intensely labeled axons and terminals were observed in the regions that contain the medullary and pontine respiratory network (Fig. 9) (Del Negro et al., 2018). Labeled fibers were not observed anterior to the parabrachial nucleus. RTN^{Nmb} fiber and terminals were present in most subregions of the LPB, with the heaviest innervation concentrated in areas reported to contained neurons that coexpress Foxp2 and Lmx1b in mouse (Karthik et al., 2022), corresponding to the Kölliker–Fuse, external lateral and lateral crescent PB (Fulwiler and Saper, 1984). Only sparse fibers were observed in the external lateral PB and the medial parabrachial nucleus (Fig. 9*E*,*M*). We also noted RTN^{Nmb} fibers in a region medial to the locus coeruleus that contained TH positive processes (Fig. 9*F*).

Within the brainstem, we observed moderate terminal fields spanning the dorsomedial edge of facial motor nucleus (Fig. 9*G*). These fibers merged caudally with the intense projection of RTN^{Nmb} neurons to the entire ventral respiratory column. RTN^{Nmb} neurons also heavily innervated the NTS, with the heaviest projections found in the ventrolateral and commissural subnuclei of the NTS (Fig. 9*H*,*M*). We also observed sparse contralateral RTN^{Nmb} projections throughout the ventral respiratory column and NTS but not to the parabrachial region. A sparse collection of axons and fibers were observed in the lateral funiculus of the cervical spinal cord with sparse terminal fields in the lateral and ventrolateral gray matter (Fig. 9*L*). We quantified the density of RTN^{Nmb} varicosities in the main targets of these efferents, finding that RTN terminals were comparably dense in the Kölliker–Fuse and ventral respiratory column, and sparser in the NTS, the perifacial region and the locus coeruleus (Fig. 9*M*).

To complement our anterograde tracing, we conducted retrograde tracing of RTN neurons (Fig. 10); we used a retrogradely transported AAV-Cre (AAV_{rg}-Cre) microinjected in a Cre- reporter mouse line and detected GFP by immunohistochemistry along with *Nmb* and *Galanin* transcripts by FISH to identify neurons. We focused on four easily distinguished locations in the ponto-medullary respiratory network: the LPB, including the Kölliker–Fuse, PreBötC, NTS, and the location of expiratory premotor neurons in the cVRG (Fig. 10*A*,*B*). Injections of AAV-Cre labeled a substantial proportion of RTN^{Nmb} neurons regardless of location (PreBötC, 74.5 ± 3.3%; LPB, 65.2 ± 2.6%; cVRG, 53.8 ± 5.5%; NTS, 37.5 ± 3.0% of total RTN^{Nmb} neurons) (Fig. 10*C*). Moreover, PreBötC, cVRG, and NTS tracing labeled an appreciable number of RTN^{Nmb} neurons contralateral to the injection site (15.5 ± 11.2%, 22.8 ± 11.7%, and 35.1 ± 5.6% of total RTN^{Nmb} neurons, respectively), whereas contralateral labeling was extremely rare following injections in the LPB (2.5 ± 1.6% of total RTN^{Nmb} neurons). Additionally, we found a small group of RTN neurons were retro-labeled following injections of AAV_{rg}-Cre in the spinal cord at T2 (8.5 and 6.8% of total Nmb^+ neurons in 2 cases), confirming the evidence from the anterograde tracing of RTN^{Nmb} neurons.

The neuropeptide Galanin is reported to be enriched in a subpopulation of CO_2-activated RTN^{Nmb} neurons that express low levels of *Nmb* transcript (Stornetta et al., 2009; Shi et al., 2017). Galanin transcript was expressed in 35.4 ± 1.7% of RTN^{Nmb} neurons, principally those with relatively low *Nmb* expression that tended to be closer to the ventral surface of the medulla (Fig. 10*E*, *F*). Within the Gal^+ population of RTN^{Nmb} neurons, virtually all

←

two-way repeated-measures ANOVA, laser-on versus CO_2 condition in hyperoxia; interaction $F_{(3,12)} = 11.21$, $p = 0.0009$. Laser-on, $F_{(1,4)} = 78.73$, $p = 0.0009$. CO_2 condition, $F_{(3,12)} = 34.77$, $p < 0.0001$. ***K***, ΔV_E during inhibition of RTN^{Nmb} neurons as a percentage of baseline in hyperoxia and hyperoxic hypercapnia. One-way repeated-measures ANOVA, $F_{(2,8)} = 24.77$, $p = 0.0004$. ***L***, Effect of RTN^{Nmb} neuron inhibition during hypoxia ($F_IO_2 = 0.1$) and during hypoxia-hypercapnia ($F_ICO_2 = 0.06$). Hypoxia blunts the effect of RTN^{Nmb} neuron inhibition, and this effect is reversed by supplementing CO_2 to the breathing mixture. ***M***, ΔV_E during inhibition of RTN^{Nmb} neuron in hypoxia and hypoxia-hypercapnia. One-way repeated-measures ANOVA, $F_{(1,6)} = 23.74$, $p = 0.0026$. *$p < 0.05$, **$p < 0.01$, **$p < 0.001$ by Bonferroni's multiple comparisons test for ***E-G***, ***J***, and by Tukey's multiple comparisons test for ***H***, ***K***, ***M***.

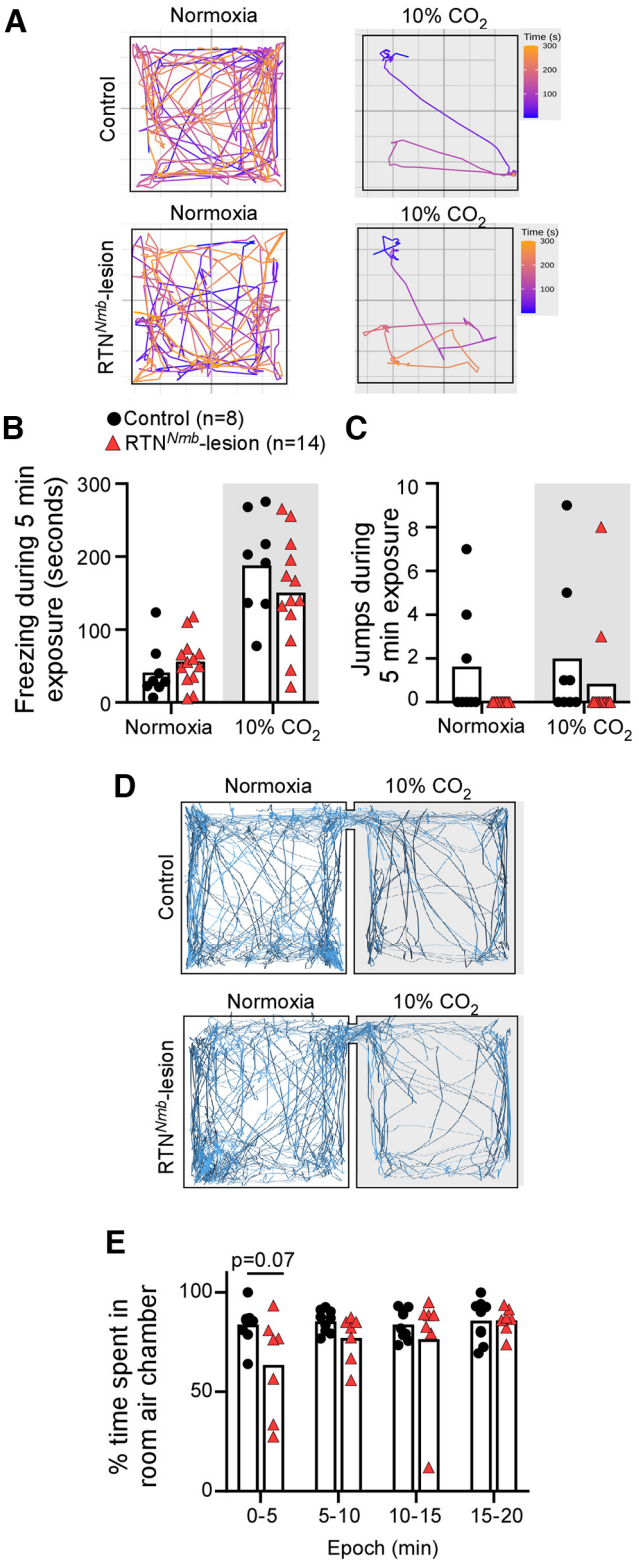

Figure 8. RTN^{Nmb}-lesion does not reduce freezing or avoidance during hypercapnia. ***A***, Example of video-tracking for controls (top panels) and RTN^{Nmb}-lesion (bottom panels) mice during normoxia and 10% CO_2 exposure in an open-field assay. ***B***, Group data for time spent freezing in 5 min during room air and 10% CO_2 conditions. Two-way repeated-measures ANOVA, RTN^{Nmb}-lesion versus CO_2 condition; interaction, $F_{(1,19)} = 2.632$, $p = 0.12$. CO_2 condition, $F_{(1,19)} = 58.58$, $p < 0.0001$. Lesion, $F_{(1,19)} = 0.3516$, $p = 0.56$. ***C***, Group data for the incidence of jumping in 5 min during normoxia and 10% CO_2 conditions. Two-way repeated-measures ANOVA, RTN^{Nmb}-lesion versus CO_2 condition; interaction, $F_{(1,19)} = 0.09873$, $p = 0.76$. CO_2 condition, $F_{(1,19)} = 0.6632$, $p = 0.43$. Lesion, $F_{(1,19)} = 4.442$, $p = 0.049$. ***D***, Example of video-tracking for controls (top) and RTN^{Nmb}-lesion (bottom) mice during a two-chamber CO_2 avoidance assay. ***E***, Group data for the % of time spent in the normoxia chamber during a 20 min period. Two-way repeated-measures ANOVA, RTN^{Nmb}-lesion versus time; interaction, $F_{(3,42)} = 1.751$, $p = 0.17$. Time, $F_{(3,42)} = 2.49$, $p = 0.074$. Lesion, $F_{(1,14)} = 3.21$, $p = 0.095$. ***E***, p indicates comparison of controls and RTN^{Nmb}-lesion mice by Sidak's multiple comparisons test.

projected to both the PreBötC and LPB (91.3 ± 5.1% and 94.9 ± 1.8%, respectively), and a majority projected to the cVRG and NTS (79.3 ± 8.9% and 59.7 ± 7.1%, respectively) (Fig. 10*D*). Together, these anatomic data demonstrate that RTN^{Nmb} neurons in mice innervate the respiratory rhythm and pattern generating network with a strong ipsilateral preference, similar to what has been described for Phox2b-expressing RTN neurons in the rat. In addition, they also project to regions that may be involved in non-respiratory functions, such as the regulation of cardiovascular function and arousal. Furthermore, RTN^{Nmb} neurons are highly collateralized, with at least one-third of these neurons having collaterals to both the PreBötC and LPB, and possibly all compartments of the respiratory network.

Discussion

Leveraging a novel transgenic line, this study reveals that RTN^{Nmb} neurons are a hub for the integration of CO_2-dependent drive to breathe. Based on the circumscribed projections of RTN^{Nmb} neurons and the persistence of the behavioral effects of high CO_2 after ablation of RTN^{Nmb} neurons, these neurons appear to be specialized for controlling the respiratory-related effects of CO_2. Following ablation of RTN^{Nmb} neurons, the contribution of oxygen-sensitive mechanisms to resting ventilation is increased markedly, suggesting that peripheral chemoreceptors, likely the carotid bodies, compensate for the loss of RTN^{Nmb} neurons. After the loss of RTN^{Nmb} neurons, a reduction in central CO_2-dependent drive to breathe coupled with a heightened role of peripheral chemoreceptors in breathing may account for breathing instability during NREMS. Similar mechanisms may also drive respiratory events during NREMS that result in sleep fragmentation in mice lacking RTN^{Nmb} neurons.

RTN^{Nmb} neurons are critical for alveolar ventilation regardless of vigilance state

RTN neurons have long been attributed a role in the HCVR but have also been viewed ultimately as redundant for eupneic ventilation at rest (Marina et al., 2010; Ramanantsoa et al., 2011; Nattie and Li, 2012; Guyenet et al., 2019). Our study finds that ablation of RTN^{Nmb} neurons in adult mice reduced resting V_E and led to a retention of CO_2 and unchanged VCO_2. As such, alveolar ventilation was reduced by 35%, which is comparable to RTN-lesion in adult rats (Souza et al., 2018). However, optogenetic inhibition of RTN^{Nmb} neurons produced a 70 ± 4% reduction in V_E in normoxic conditions and complete apnea in hyperoxic conditions, which indicates that that the 35% reduction in alveolar ventilation in RTN^{Nmb}-lesion mice relative to controls is likely an underestimation of RTN^{Nmb} neuron contribution to eupneic respiratory drive. Importantly, the effects of ablation or optogenetic inhibition of RTN^{Nmb} neurons on V_E were comparable in absolute terms during waking and NREMS, indicating that the RTN^{Nmb} neuron contribution to breathing does not significantly interact with the "waking drive to breathe" (Shea, 1996; Khoo, 2000). Thus, our data demonstrate that RTN^{Nmb} neurons regulate respiratory homeostasis across vigilance states, with a more pronounced contribution to V_E during NREMS.

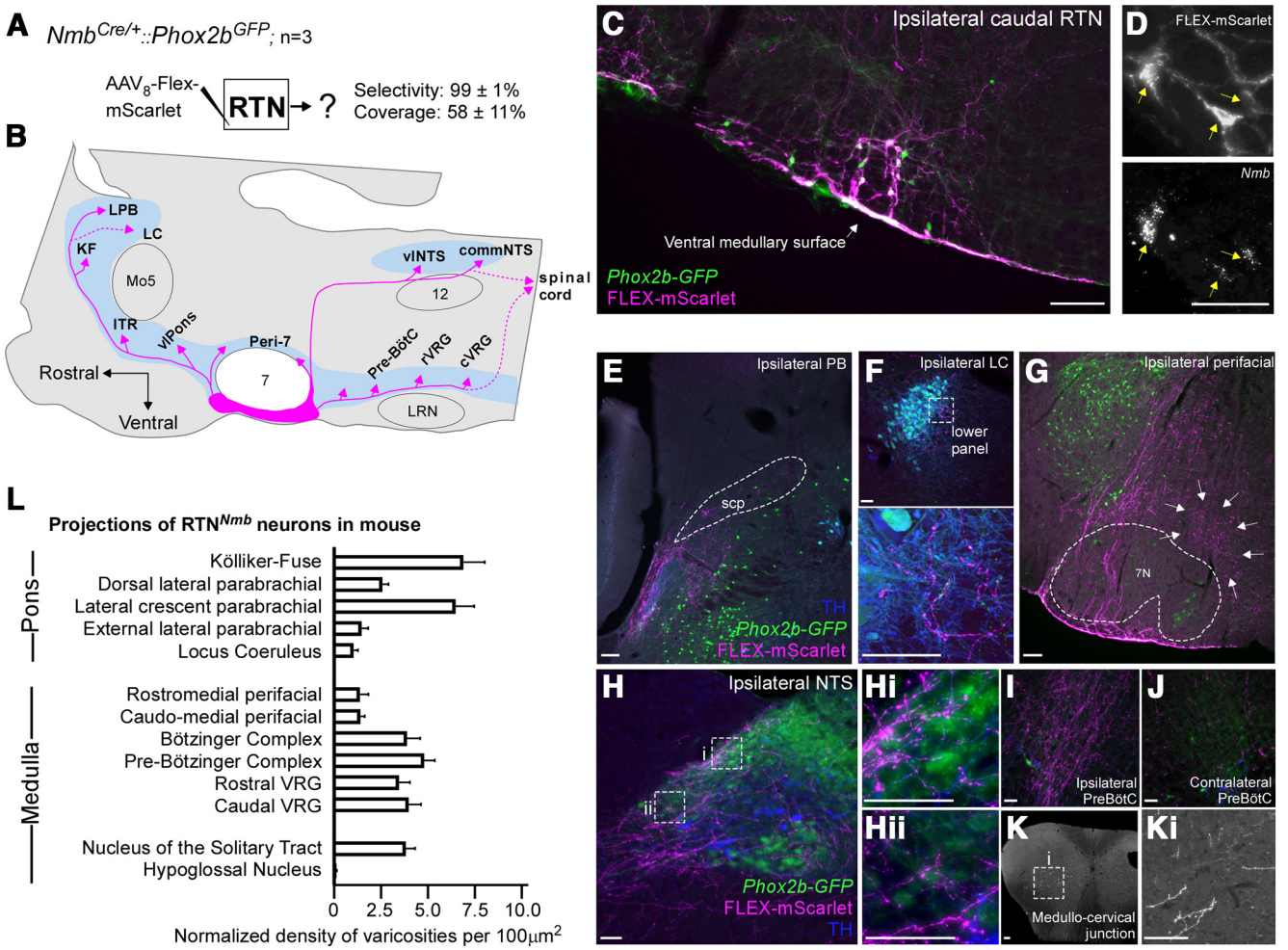

Figure 9. RTN^{Nmb} neurons innervate the ponto-medullary respiratory network. ***A***, Experimental approach to label the efferents of RTN^{Nmb} neurons. ***B***, Graphic summary of projections of RTN^{Nmb} neurons. ***C***, Image of RTN Nmb neurons at the site of virus injection. ***D***, ISH showing co-expression of mScarlet (upper panel) and Nmb mRNA (lower panel). ***E***, Image of RTN^{Nmb} neurons projecting to the LPB. ***F***, Image of projections of RTN^{Nmb} neurons to locus coeruleus labeled with TH and Phox2b-GFP. ***G***, Image of projections of RTN^{Nmb} neurons to the dorsomedial perifacial region (indicated by white arrows). This projection extended the rostro-caudal length of the facial motor nucleus. ***H***, Image of projections of RTN^{Nmb} neurons to the NTS; ***Hi***, ***Hii***, Insets. ***I***, ***J***, Images of projections of RTN^{Nmb} neurons to the PreBötC, ipsilateral to the injection site in ***I*** and contralateral to the injections site in ***J***. ***K***. Images of labeled axons of RTN^{Nmb} neurons in the upper cervical spinal cord. ***L***, Normalized density of varicosities per 100 mm^2 across different pontomedullary regions. Scale bars: all photomicrographs, 100 μm. ITR, Intertrigeminal region.

This result is consistent with the notion that hypoventilation during sleep in individuals with CCHS could be partly because of a disruption of RTN^{Nmb} neurons.

RTN^{Nmb} neurons stabilize breathing during NREMS

Robust and regular respiratory motor activity is necessary for optimal gas exchange, and ventilatory instability is an important factor contributing to the pathogenesis of sleep-related breathing disorders (Javaheri et al., 2017; Orr et al., 2017). In this study, we observed increased breathing variability in RTN^{Nmb}-lesion mice that was clearest during NREMS. Recent studies (Cleary et al., 2021; Ferreira et al., 2022) corroborate our findings, and suggest that breathing instability is a consistent phenotype caused by RTN dysfunction in adult mice. Conversely, RTN-lesion in rats does not cause respiratory instability in normoxic conditions (Souza et al., 2018). However, this could be explained by the countervailing effect of damage to respiratory centers, such as the Bötzinger complex and possibly other neurons (Souza et al., 2019).

Breathing instability in RTN^{Nmb}-lesion mice was exacerbated at the onset of NREMS, which is notable because periodic breathing in humans during hypoxia and in central sleep apnea occurs predominantly during light NREMS (Javaheri and Dempsey, 2013). We also observed an increase in respiratory-related microarousals in normoxic conditions in RTN^{Nmb}-lesion mice, suggesting that respiratory disturbances caused by a loss of RTN^{Nmb} neurons are significant enough to disrupt NREMS. We did not observe apneas in RTN^{Nmb}-lesion mice under normoxic conditions, which is presumably because of elevated peripheral chemoreceptor activity. This observation is supported by the appearance of apneas in RTN^{Nmb}-lesion mice under hyperoxia.

The administration of CO_2 or lowering arterial pH with acetazolamide stabilizes erratic breathing pattern in healthy humans during hypoxia and at high altitude (Berssenbrugge et al., 1983; Fan et al., 2012), and in patients with obstructive sleep apnea (Xie et al., 2013) and Cheyne-Stokes breathing (Lorenzi-Filho et al., 1999; Javaheri, 2006). However, breathing instability in RTN^{Nmb}-lesion mice was not corrected by increasing inspired CO_2. Together, these data provide evidence that RTN^{Nmb} neurons mediate the stabilizing effect of CO_2 on breathing and suggest that a loss of this mechanism leads to sleep-disordered breathing in mice.

What mechanisms cause unstable breathing in RTN^{Nmb}-lesion mice? Periodic breathing in humans and experimental animals is thought to involve interactions between the apneic threshold, the sensitivity of the HCVR (i.e., loop gain), transient

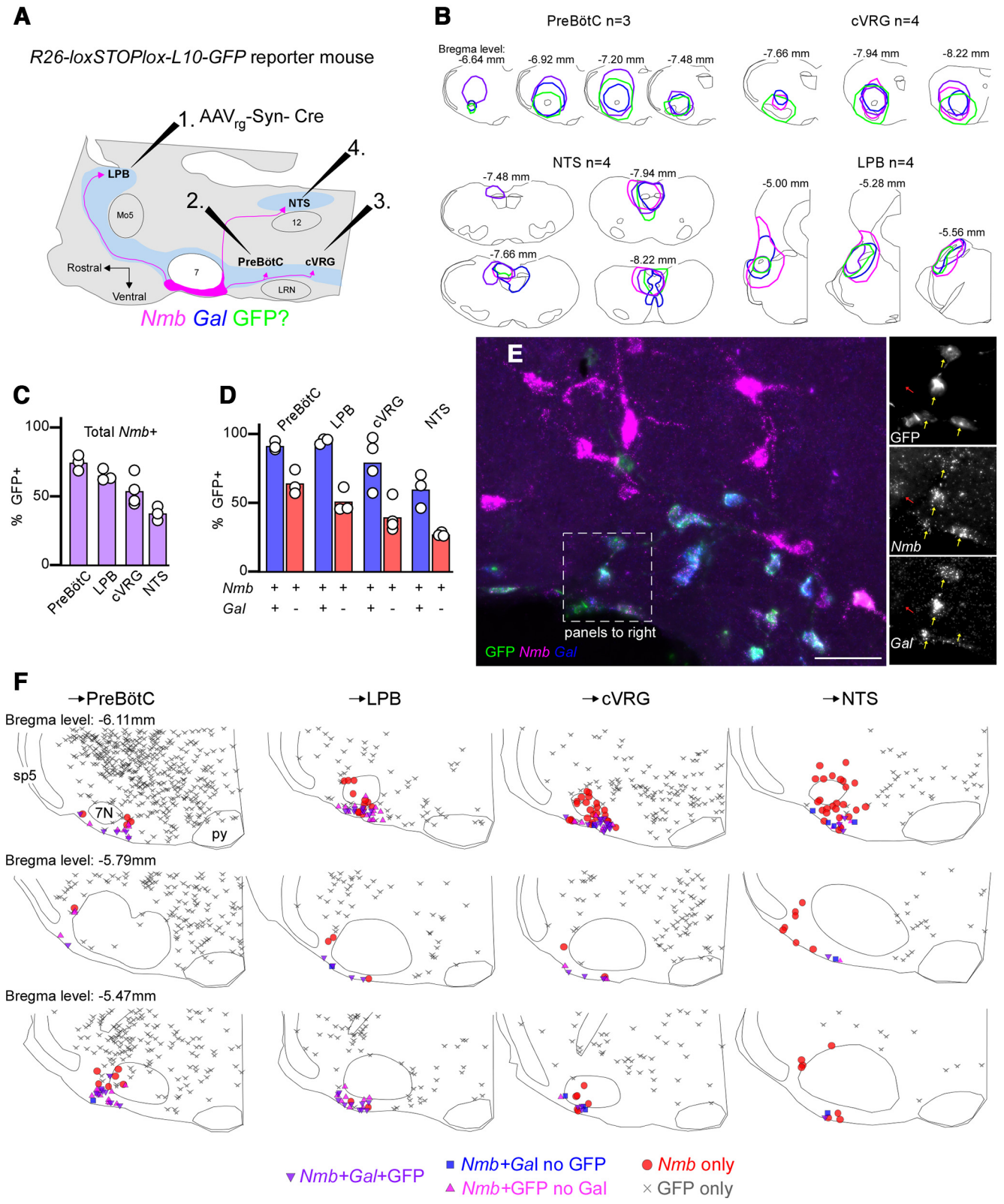

Figure 10. RTN neuron projections to the ponto-medullary respiratory network are highly collateralized. ***A***, Experimental approach to retrogradely label RTN^{Nmb} neurons using a Cre-reporter mouse. ***B***, Location and distribution of AAV$_{rg}$-Cre injections. ***C***, Group data percent of RTN^{Nmb} neurons that innervate the PreBötC, LPB, cVRG, and NTS. ***D***, Same data as in ***C***, except segregated according to the presence or absence of Galanin transcript (*Gal*). ***E***, Image of retrograde-labeled RTN^{Nmb} neurons after injections in the cVRG. RTN^{Nmb} neurons that were *Gal*- were less commonly labeled that RTN^{Nmb} neurons that were *Gal*$^{+}$, and that *Gal*$^{+}$ often expressed low levels of *Nmb*. Scale bar, 100 μm. ***F***, Distribution of retrograde-labeled RTN^{Nmb} neuron from a representative case from each targeted region.

arousals, and cerebral blood flow (Ainslie et al., 2013; Javaheri and Dempsey, 2013). Among these possibilities, an elevation in apneic threshold is particularly plausible given that RTN^{Nmb}-lesion mice are unresponsive to CO_2, and previous studies in rats show that RTN-lesion raises the apneic threshold (Takakura et al., 2008). Furthermore, we observed evidence indicative of enhanced peripheral chemoreceptor activity and sensitivity in RTN^{Nmb}-lesion mice, which contributes to periodic breathing in humans and dogs (Javaheri and Dempsey, 2013). The carotid body (Lopez-Barneo, 2022), which detects O_2, CO_2, and H^+, is the most likely source of compensatory respiratory drive in RTN^{Nmb}-lesion mice, though not the only possibility (aortic bodies and brainstem mechanisms) (Lahiri and Forster, 2003; Angelova et al., 2015; Gourine and Funk, 2017; Uchiyama et al., 2020). Thus, unstable breathing in RTN^{Nmb}-lesion mice could be caused by an elevated apneic threshold compounded by carotid body hyperactivity and hypersensitivity. Transient arousal and altered cerebral blood flow may also contribute to breathing instability in this model as an effect secondary to the respiratory dysfunction in RTN^{Nmb}-lesion mice.

RTN^{Nmb} neurons are specialized for the respiratory regulation of CO_2

RTN^{Nmb} neurons have been proposed to have two nonmutually exclusive functions: Shi et al. (2017) proposed that *Nmb* is expressed by RTN chemoreceptor neurons (Guyenet et al., 2019), whereas Li et al. (2016, 2020) proposed that *Nmb* identifies perifacial neurons that stimulate sighs. In the present study, selective ablation of RTN^{Nmb} neurons (1) elevated arterial P_{CO_2} by 10 mmHg, (2) largely eliminated the HCVR, and (3) increased spontaneous sighs. These results broadly support the interpretation of Shi et al. (2017) but are not consistent with the results of Li et al. (2020) who used chemogenetics to silence RTN^{Nmb} neurons and found no changes in minute-ventilation and a reduction in sigh frequency. This discrepancy may be attributable to differences in the transgenic model and approach used, and in the case of sigh frequency, the activation of O_2-sensitive mechanisms that prevent alveoli collapse in the lungs (atelectasis). Notably, RTN^{Nmb} neurons appear not to contribute to hypoxia-induced sighing in mice (Souza et al., 2018; Li et al., 2020; current study), which may instead be mediated by Grp-expressing neurons of the NTS (Yao et al., 2023).

The reduction in the HCVR in RTN^{Nmb}-lesion mice largely aligns with previous studies that use genetic deletion, inhibition, or lesion of the RTN Phox2b neurons (Marina et al., 2010; Takakura et al., 2014; Ruffault et al., 2015; Souza et al., 2018). However, we observed a substantially larger reduction in the HCVR than many previous studies, which we attribute to the selectivity and efficiency of the approach used in this study and the absence of developmental compensation. Importantly, the reduction in the HCVR in RTN^{Nmb}-lesion mice could be because of an attenuation of active expiration, which is an important mechanism for increasing V_T during hypercapnia. Anatomically, RTN^{Nmb} neurons are found in both the ventral and lateral parafacial region, which are important for active expiration (Pagliardini et al., 2011; Huckstepp et al., 2015). Moreover, functional studies using the Phox2b-promoter, PRSx8, to target RTN neurons in rats show that the selective activation of RTN neurons drives active expiration (Souza et al., 2020) and inhibition of RTN neurons blocks active expiration in anesthetized and reduced preparations (Marina et al., 2010). As such, the data support the interpretation that active expiration is attenuated in RTN^{Nmb}-lesion mice. However, direct recordings of abdominal activity during hypercapnia are needed to verify this interpretation. In contrast to the reduction in the HCVR, RTN^{Nmb}-lesion mice had a robust behavioral response to high CO_2, which suggests that RTN^{Nmb}-lesion selectively disrupts respiratory-related responses to hypercapnia. Consistent with this notion, our data show that RTN^{Nmb} neurons projects densely and almost exclusively to the respiratory-related regions in the pons and medulla. These projections are highly collateralized and generally conform to the descriptions of the connectivity of Phox2b-expressing RTN neurons in rats (Abbott et al., 2009; Souza et al., 2020). Given their anatomy, RTN^{Nmb} neurons are well placed to stimulate respiratory circuits that promote alveolar gas-exchange. Thus, our results provide essential functional and anatomic evidence for the assertion that perifacial *Nmb* expression in adult mice identifies CO_2-activated Phox2b-expressing central chemoreceptor neurons that contribute to the respiratory regulation of arterial P_{CO_2} and pH.

Compensatory responses after RTN^{Nmb} ablation in mice

This study shows that the loss of RTN neurons produces alveolar hypoventilation and fully compensated respiratory acidosis, which could involve several physiological adaptations (Cummins et al., 2020). Our data indicate that the renal retention of bicarbonate normalizes arterial pH and respiratory homeostasis establishes at a new set point for P_{O_2}/P_{CO_2}. The resetting of respiratory homeostasis appears to be mediated by O_2-dependent respiratory drive and, to a lesser extent, wake-active drive that compensates for the loss of CO_2-dependent respiratory drive. The greater effect of hyperoxia on V_E in RTN^{Nmb}-lesion mice suggests that there is a reduction in CO_2 drive to breath at equilibrium, but our data suggest that there is a weak but persistent effect of CO_2 on breathing. First, there was a small residual HCVR under normoxic and hyperoxic conditions in RTN^{Nmb}-lesion mice. Second, breathing at rest persisted under hyperoxic conditions in RTN^{Nmb}-lesion mice, although this interpretation is predicated on the assumption that hyperoxia effectively silences O_2-sensing mechanisms in RTN^{Nmb}-lesion mice. Finally, post-hypoxia breathing instability, which we attribute to CO_2 chemoreceptor silencing caused by hyperventilation-induced hypocapnia/alkalosis (Lydic et al., 2002; but see Millhorn et al., 1984; Gallman and Millhorn, 1988), was similar in RTN^{Nmb}-lesion and control mice. In sum, respiratory homeostasis in RTN^{Nmb}-lesion mice is largely driven by the O_2 homeostasis, but a small component of CO_2- and/or H^+-dependent respiratory drive may still contribute to alveolar ventilation and respiratory homeostasis.

In conclusion, the selective ablation of RTN^{Nmb} neurons causes hypoventilation at rest and virtually eliminates the HCVR. Moreover, we demonstrated that disrupting RTN^{Nmb} neurons causes highly unstable breathing patterns, particularly during sleep, which raises the possibility that a change in RTN^{Nmb} activity could be important in the etiology of certain forms of sleep-disordered breathing in humans. The potent respiratory effect of deleting RTN^{Nmb} neurons appears to stem from a breakdown in the relationship between P_{aCO_2} and ventilation that exists in intact conditions, which results in respiratory homeostasis driven by O_2-dependent mechanisms.

References

Abbott SB, Souza G (2021) Chemoreceptor mechanisms regulating CO(2)-induced arousal from sleep. J Physiol 599:2559–2571.

Abbott SB, Stornetta RL, Fortuna MG, Depuy SD, West GH, Harris TE, Guyenet PG (2009) Photostimulation of retrotrapezoid nucleus phox2b-expressing neurons in vivo produces long-lasting activation of breathing in rats. J Neurosci 29:5806–5819.

Abbott SB, Stornetta RL, Coates MB, Guyenet PG (2011) Phox2b-expressing neurons of the parafacial region regulate breathing rate, inspiration, and expiration in conscious rats. J Neurosci 31:16410–16422.

Abbott SB, DePuy SD, Nguyen T, Coates MB, Stornetta RL, Guyenet PG (2013) Selective optogenetic activation of rostral ventrolateral medullary catecholaminergic neurons produces cardiorespiratory stimulation in conscious mice. J Neurosci 33:3164–3177.

Ainslie PN, Lucas SJ, Burgess KR (2013) Breathing and sleep at high altitude. Respir Physiol Neurobiol 188:233–256.

Amiel J, Laudier B, Attie-Bitach T, Trang H, de Pontual L, Gener B, Trochet D, Etchevers H, Ray P, Simonneau M, Vekemans M, Munnich A, Gaultier C, Lyonnet S (2003) Polyalanine expansion and frameshift mutations of the paired-like homeobox gene PHOX2B in congenital central hypoventilation syndrome. Nat Genet 33:459–461.

Angelova PR, Kasymov V, Christie I, Sheikhbahaei S, Turovsky E, Marina N, Korsak A, Zwicker J, Teschemacher AG, Ackland GL, Funk GD, Kasparov S, Abramov AY, Gourine AV (2015) Functional oxygen sensitivity of astrocytes. J Neurosci 35:10460–10473.

Basting TM, Burke PG, Kanbar R, Viar KE, Stornetta DS, Stornetta RL, Guyenet PG (2015) Hypoxia silences retrotrapezoid nucleus respiratory chemoreceptors via alkalosis. J Neurosci 35:527–543.

Berssenbrugge A, Dempsey J, Iber C, Skatrud J, Wilson P (1983) Mechanisms of hypoxia-induced periodic breathing during sleep in humans. J Physiol 343:507–524.

Blain GM, Smith CA, Henderson KS, Dempsey JA (2009) Contribution of the carotid body chemoreceptors to eupneic ventilation in the intact, unanesthetized dog. J Appl Physiol 106:1564–1573.

Bradski G (2000) Dr. Dobb's Journal of Software Tools. An open-source library for processing image data. 25:120–125. https://github.com/opencv/opencv/wiki/CiteOpenCV.

Burke PG, Kanbar R, Basting TM, Hodges WM, Viar KE, Stornetta RL, Guyenet PG (2015) State-dependent control of breathing by the retrotrapezoid nucleus. J Physiol 593:2909–2926.

Cleary CM, James S, Maher BJ, Mulkey DK (2021) Disordered breathing in a Pitt-Hopkins syndrome model involves Phox2b-expressing parafacial neurons and aberrant Nav1.8 expression. Nat Commun 12:5962.

Cummins EP, Strowitzki MJ, Taylor CT (2020) Mechanisms and consequences of oxygen and carbon dioxide sensing in mammals. Physiol Rev 100:463–488.

Del Negro CA, Funk GD, Feldman JL (2018) Breathing matters. Nat Rev Neurosci 19:351–367.

Dempsey JA (2019) Central sleep apnea: misunderstood and mistreated! F1000Res 8:981.

Dubreuil V, Thoby-Brisson M, Rallu M, Persson K, Pattyn A, Birchmeier C, Brunet JF, Fortin G, Goridis C (2009) Defective respiratory rhythmogenesis and loss of central chemosensitivity in Phox2b mutants targeting retrotrapezoid nucleus neurons. J Neurosci 29:14836–14846.

Fan JL, Burgess KR, Thomas KN, Lucas SJ, Cotter JD, Kayser B, Peebles KC, Ainslie PN (2012) Effects of acetazolamide on cerebrovascular function and breathing stability at 5050 m. J Physiol 590:1213–1225.

Fenno LE, Ramakrishnan C, Kim YS, Evans KE, Lo M, Vesuna S, Inoue M, Cheung KY, Yuen E, Pichamoorthy N, Hong AS, Deisseroth K (2020) Comprehensive dual- and triple-feature intersectional single-vector delivery of diverse functional payloads to cells of behaving mammals. Neuron 107:836–853.e811.

Ferreira CB, Silva TM, Silva PE, Castro CL, Czeisler C, Otero JJ, Takakura AC, Moreira TS (2022) Phox2b mutation mediated by Atoh1 expression impaired respiratory rhythm and ventilatory responses to hypoxia and hypercapnia. Elife 11:e73130.

Franklin KBJ, Paxinos G (2013) Paxinos and Franklin's The mouse brain in stereotaxic coordinates, Fourth edition. Amsterdam: Academic Press, an imprint of Elsevier.

Fulwiler CE, Saper CB (1984) Subnuclear organization of the efferent connections of the parabrachial nucleus in the rat. Brain Res 319:229–259.

Gallman EA, Millhorn DE (1988) Two long-lasting central respiratory responses following acute hypoxia in glomectomized cats. J Physiol 395:333–347.

Gestreau C, Heitzmann D, Thomas J, Dubreuil V, Bandulik S, Reichold M, Bendahhou S, Pierson P, Sterner C, Peyronnet-Roux J, Benfriha C, Tegtmeier I, Ehnes H, Georgieff M, Lesage F, Brunet JF, Goridis C, Warth R, Barhanin J (2010) Task2 potassium channels set central respiratory CO_2 and O_2 sensitivity. Proc Natl Acad Sci USA 107:2325–2330.

Getsy PM, Davis J, Coffee GA, May WJ, Palmer LA, Strohl KP, Lewis SJ (2014) Enhanced non-eupneic breathing following hypoxic, hypercapnic or hypoxic-hypercapnic gas challenges in conscious mice. Respir Physiol Neurobiol 204:147–159.

Gourine AV, Funk GD (2017) On the existence of a central respiratory oxygen sensor. J Appl Physiol 123:1344–1349.

Gourine AV, Dale N (2022) Brain H(+)/CO(2) sensing and control by glial cells. Glia 70:1520–1535.

Guyenet PG, Bayliss DA (2022) Central respiratory chemoreception. Handb Clin Neurol 188:37–72.

Guyenet PG, Bayliss DA, Stornetta RL, Kanbar R, Shi Y, Holloway BB, Souza G, Basting TM, Abbott SB, Wenker IC (2018) Interdependent feedback regulation of breathing by the carotid bodies and the retrotrapezoid nucleus. J Physiol 596:3029–3042.

Guyenet PG, Stornetta RL, Souza G, Abbott SB, Shi Y, Bayliss DA (2019) The retrotrapezoid nucleus: central chemoreceptor and regulator of breathing automaticity. Trends Neurosci 42:807–824.

Huckstepp RT, Cardoza KP, Henderson LE, Feldman JL (2015) Role of parafacial nuclei in control of breathing in adult rats. J Neurosci 35:1052–1067.

Javaheri S (2006) Acetazolamide improves central sleep apnea in heart failure: a double-blind, prospective study. Am J Respir Crit Care Med 173:234–237.

Javaheri S, Dempsey JA (2013) Central sleep apnea. Compr Physiol 3:141–163.

Javaheri S, Barbe F, Campos-Rodriguez F, Dempsey JA, Khayat R, Javaheri S, Malhotra A, Martinez-Garcia MA, Mehra R, Pack AI, Polotsky VY, Redline S, Somers VK (2017) Sleep apnea: types, mechanisms, and clinical cardiovascular consequences. J Am Coll Cardiol 69:841–858.

Karthik S, Huang D, Delgado Y, Laing JJ, Peltekian L, Iverson GN, Grady F, Miller RL, McCann CM, Fritzsch B, Iskusnykh IY, Chizhikov VV, Geerling JC (2022) Molecular ontology of the parabrachial nucleus. J Comp Neurol 530:1658–1699.

Khoo MC (2000) Determinants of ventilatory instability and variability. Respir Physiol 122:167–182.

Kumar NN, Velic A, Soliz J, Shi Y, Li K, Wang S, Weaver JL, Sen J, Abbott SB, Lazarenko RM, Ludwig MG, Perez-Reyes E, Mohebbi N, Bettoni C, Gassmann M, Suply T, Seuwen K, Guyenet PG, Wagner CA, Bayliss DA (2015) PHYSIOLOGY. Regulation of breathing by CO(2) requires the proton-activated receptor GPR4 in retrotrapezoid nucleus neurons. Science 348:1255–1260.

Lahiri S, Forster RE 2nd (2003) CO2/H(+) sensing: peripheral and central chemoreception. Int J Biochem Cell Biol 35:1413–1435.

Lazarenko RM, Milner TA, Depuy SD, Stornetta RL, West GH, Kievits JA, Bayliss DA, Guyenet PG (2009) Acid sensitivity and ultrastructure of the retrotrapezoid nucleus in Phox2b-EGFP transgenic mice. J Comp Neurol 517:69–86.

Li P, Janczewski WA, Yackle K, Kam K, Pagliardini S, Krasnow MA, Feldman JL (2016) The peptidergic control circuit for sighing. Nature 530:293–297.

Li P, Li SB, Wang X, Phillips CD, Schwarz LA, Luo L, de Lecea L, Krasnow MA (2020) Brain circuit of claustrophobia-like behavior in mice identified by upstream tracing of sighing. Cell Rep 31:107779.

Lopez-Barneo J (2022) Neurobiology of the carotid body. Handb Clin Neurol 188:73–102.

Lorenzi-Filho G, Rankin F, Bies I, Douglas Bradley T (1999) Effects of inhaled carbon dioxide and oxygen on cheyne-stokes respiration in patients with heart failure. Am J Respir Crit Care Med 159:1490–1498.

Lydic R, Douglas CL, Baghdoyan HA (2002) Microinjection of neostigmine into the pontine reticular formation of C57BL/6J mouse enhances rapid eye movement sleep and depresses breathing. Sleep 25:835–841.

Marina N, Abdala AP, Trapp S, Li A, Nattie EE, Hewinson J, Smith JC, Paton JF, Gourine AV (2010) Essential role of Phox2b-expressing ventrolateral brainstem neurons in the chemosensory control of inspiration and expiration. J Neurosci 30:12466–12473.

Millhorn DE, Eldridge FL, Kiley JP, Waldrop TG (1984) Prolonged inhibition of respiration following acute hypoxia in glomectomized cats. Respir Physiol 57:331–340.

Nattie E, Li A (2012) Central chemoreceptors: locations and functions. Compr Physiol 2:221–254.

Orr JE, Malhotra A, Sands SA (2017) Pathogenesis of central and complex sleep apnoea. Respirology 22:43–52.

Pagliardini S, Janczewski WA, Tan W, Dickson CT, Deisseroth K, Feldman JL (2011) Active expiration induced by excitation of ventral medulla in adult anesthetized rats. J Neurosci 31:2895–2905.

Panadeiro V, Rodriguez A, Henry J, Wlodkowic D, Andersson M (2021) A review of 28 free animal-tracking software applications: current features and limitations. Lab Anim (NY) 50:246–254.

Ridler TW, Calvard S (1978) Picture thresholding using an iterative selection method. IEEE Trans Syst Man Cybern B Cybern 8:630–632.

Ramanantsoa N, Hirsch MR, Thoby-Brisson M, Dubreuil V, Bouvier J, Ruffault PL, Matrot B, Fortin G, Brunet JF, Gallego J, Goridis C (2011) Breathing without CO(2) chemosensitivity in conditional Phox2b mutants. J Neurosci 31:12880–12888.

Ruffault PL, D'Autreaux F, Hayes JA, Nomaksteinsky M, Autran S, Fujiyama T, Hoshino M, Hagglund M, Kiehn O, Brunet JF, Fortin G, Goridis C (2015) The retrotrapezoid nucleus neurons expressing Atoh1 and Phox2b are essential for the respiratory response to CO(2). Elife 4: e07051.

Schindelin J, Arganda-Carreras I, Frise E, Kaynig V, Longair M, Pietzsch T, Preibisch S, Rueden C, Saalfeld S, Schmid B, Tinevez J-Y, White DJ, Hartenstein V, Eliceiri K, Tomancak P, Cardona A, (2012) Fiji: an open-source platform for biological-image analysis. Nat Methods 9:676–682.

Shea SA (1996) Behavioural and arousal-related influences on breathing in humans. Exp Physiol 81:1–26.

Shi Y, Stornetta RL, Stornetta DS, Onengut-Gumuscu S, Farber EA, Turner SD, Guyenet PG, Bayliss DA (2017) Neuromedin B expression defines the mouse retrotrapezoid nucleus. J Neurosci 37:11744–11757.

Silva JN, Tanabe FM, Moreira TS, Takakura AC (2016) Neuroanatomical and physiological evidence that the retrotrapezoid nucleus/parafacial region regulates expiration in adult rats. Respir Physiol Neurobiol 227:9–22.

Smith CA, Forster HV, Blain GM, Dempsey JA (2010) An interdependent model of central/peripheral chemoreception: evidence and implications for ventilatory control. Respir Physiol Neurobiol 173:288–297.

Souza G, Kanbar R, Stornetta DS, Abbott SB, Stornetta RL, Guyenet PG (2018) Breathing regulation and blood gas homeostasis after near complete lesions of the retrotrapezoid nucleus in adult rats. J Physiol 596:2521–2545.

Souza G, Stornetta RL, Stornetta DS, Abbott SB, Guyenet PG (2019) Contribution of the retrotrapezoid nucleus and carotid bodies to hypercapnia- and hypoxia-induced arousal from sleep. J Neurosci 39:9725–9737.

Souza G, Stornetta RL, Stornetta DS, Abbott SB, Guyenet PG (2020) Differential contribution of the retrotrapezoid nucleus and C1 neurons to active expiration and arousal in rats. J Neurosci 40:8683–8697.

Stornetta RL, Spirovski D, Moreira TS, Takakura AC, West GH, Gwilt JM, Pilowsky PM, Guyenet PG (2009) Galanin is a selective marker of the retrotrapezoid nucleus in rats. J Comp Neurol 512:373–383.

Takakura AC, Moreira TS, Stornetta RL, West GH, Gwilt JM, Guyenet PG (2008) Selective lesion of retrotrapezoid Phox2b-expressing neurons raises the apnoeic threshold in rats. J Physiol 586:2975–2991.

Takakura AC, Barna BF, Cruz JC, Colombari E, Moreira TS (2014) Phox2b-expressing retrotrapezoid neurons and the integration of central and peripheral chemosensory control of breathing in conscious rats. Exp Physiol 99:571–585.

Taugher RJ, Dlouhy BJ, Kreple CJ, Ghobbeh A, Conlon MM, Wang Y, Wemmie JA (2020) The amygdala differentially regulates defensive behaviors evoked by CO(2). Behav Brain Res 377:112236.

Uchiyama M, Nakao A, Kurita Y, Fukushi I, Takeda K, Numata T, Tran HN, Sawamura S, Ebert M, Kurokawa T, Sakaguchi R, Stokes AJ, Takahashi N, Okada Y, Mori Y (2020) O(2)-dependent protein internalization underlies astrocytic sensing of acute hypoxia by restricting multimodal TRPA1 channel responses. Curr Biol 30:3378–3396.e3377.

Vollmer LL, Ghosal S, McGuire JL, Ahlbrand RL, Li KY, Santin JM, Ratliff-Rang CA, Patrone LG, Rush J, Lewkowich IP, Herman JP, Putnam RW, Sah R (2016) Microglial acid sensing regulates carbon dioxide-evoked fear. Biol Psychiatry 80:541–551.

Weese-Mayer DE, Berry-Kravis EM, Ceccherini I, Keens TG, Loghmanee DA, Trang H, ATS Congenital Central Hypoventilation Syndrome Subcommittee (2010) An official ATS clinical policy statement. Congenital central hypoventilation syndrome: genetic basis, diagnosis, and management. Am J Respir Crit Care Med 181:626–644.

Xie A, Teodorescu M, Pegelow DF, Teodorescu MC, Gong Y, Fedie JE, Dempsey JA (1985) Effects of stabilizing or increasing respiratory motor outputs on obstructive sleep apnea. J Appl Physiol 115:22–33.

Yamauchi M, Dostal J, Strohl KP (2007) Acetazolamide protects against post-hypoxic unstable breathing in the C57BL/6J mouse. J Appl Physiol 103:1263–1268.

Yao Y, Chen J, Li X, Chen ZF, Li P (2023) A carotid body-brainstem neural circuit mediates sighing in hypoxia. Curr Biol 33:827–837.e4.

Ziemann AE, Allen JE, Dahdaleh NS, Drebot II, Coryell MW, Wunsch AM, Lynch CM, Faraci FM, Howard MA 3rd, Welsh MJ, Wemmie JA (2009) The amygdala is a chemosensor that detects carbon dioxide and acidosis to elicit fear behavior. Cell 139:1012–1021.